8-1-2016

Factors Controlling Stratocumulus Cloud Lifetime Over Coastal Land

Mohamed S. Ghonima
University of California

Thijs Heus
Cleveland State University, t.heus@csuohio.edu

Joel R. Norris
University of California

Jan Kleissl
University of California

Factors Controlling Stratocumulus Cloud Lifetime over Coastal Land

MOHAMED S. GHONIMA

Department of Mechanical and Aerospace Engineering, University of California, San Diego, La Jolla, California

THIJS HEUS

Department of Physics, Cleveland State University, Cleveland, Ohio

JOEL R. NORRIS

Scripps Institution of Oceanography, University of California, San Diego, La Jolla, California

JAN KLEISSL

Department of Mechanical and Aerospace Engineering, University of California, San Diego, La Jolla, California

(Manuscript received 6 August 2015, in final form 10 March 2016)

ABSTRACT

The breakup of stratocumulus clouds over coastal land areas is studied using a combination of large-eddy simulations (LESs) and mixed-layer models (MLMs) with a focus on mechanisms regulating the timing of the breakup. In contrast with stratocumulus over ocean, strong sensible heat flux over land prevents the cloud layer from decoupling during day. As the cloud thins during day, turbulence generated by surface flux becomes larger than turbulence generated by longwave cooling across the cloud layer. To capture this shift in turbulence generation in the MLM, an existing entrainment parameterization is extended. The MLM is able to mimic cloud evolution for a variety of Bowen ratios, but only after this modification of the entrainment parameterization. Cloud lifetime depends on a combination of the cloud-top entrainment flux, the Bowen ratio of the surface, and the strength of advection of cool ocean air by the sea breeze. For dry land surface conditions, the authors' MLM suggests a breakup time a few hours after sunrise. For relatively wet land surface conditions, the cloud layer briefly breaks into partly cloudy conditions during midday, and the stratocumulus cloud reforms in the evening.

1. Introduction

Stratocumulus clouds play an important role in Earth's energy balance, hydrological cycle, and applications. Because of the prevalence and high albedo of stratocumulus clouds, small changes in stratocumulus cover and thickness can lead to strong responses in Earth's climate (e.g., Randall et al. 1984). However, climate models are unable to accurately model stratocumulus clouds (Bony and Dufresne 2005). Because of the stark contrast between cloud albedo and ocean surface albedo, the majority of research on stratocumulus clouds has focused on observing, measuring, and modeling marine stratocumulus clouds in the subtropics [Wood (2012) and references therein] or as part of postfrontal systems (Mechem et al. 2010a,2010b). Although receiving less attention, stratocumulus clouds are also abundant over coastal land areas that are frequently well populated (Hilliker and Fritsch 1999; Iacobellis and Cayan 2013; Mathiesen and Kleissl 2011).

The stratocumulus topped boundary layer (STBL) over ocean and land is characterized by a strong temperature inversion that limits the vertical mixing of cool moist air in the boundary layer with warm dry air aloft (Klein and Hartmann 1993). This inversion forms when

Corresponding author address: Mohamed Ghonima, University of California, San Diego, 9500 Gilman Dr., Bldg. EBU II, Room 304, La Jolla, CA 92093-0411.
E-mail: mghonima@ucsd.edu

DOI: 10.1175/JAS-D-15-0228.1

warm dry air descending from aloft in a high pressure cell interfaces with cool moist air near the surface. Turbulence in the STBL transports water from surface to the cloud layer and promotes entrainment of dry air from the free troposphere. Nocturnally, cloud-top longwave radiative cooling is the primary driver of turbulence in the boundary layer, often resulting in a well-mixed layer that acts to maintain the stratocumulus cloud layer (Lilly 1968). During the day, solar absorption within the cloud counteracts the longwave cooling, thereby reducing the convective mixing. Thus, stratocumulus clouds over the ocean usually attain maximum coverage and thickness just before dawn, minimum coverage and thickness in the early afternoon, and exhibit a marked diurnal cycle (Wood et al. 2002).

The stratocumulus diurnal cycle is even stronger over land. Since land surfaces have a lower heat capacity than ocean, a significant portion of incoming solar radiation is reemitted as sensible and latent heat flux. The stronger surface flux leads to substantial warming and moistening of the STBL over land compared to ocean. Furthermore, during day the surface buoyancy flux becomes the main driver of turbulence in the STBL, offsetting the decrease in turbulence generated by longwave cooling. Hence, cloud-top entrainment velocities over land can exceed $10\,\mathrm{mm\,s^{-1}}$ during midday (Mechem et al. 2010b), in comparison to entrainment velocities that rarely exceed $5\,\mathrm{mm\,s^{-1}}$ over ocean (Stevens 2002). Consequently, warming through solar absorption, surface sensible heat flux, and entrainment of drier warmer air aloft are the main causes of daytime cloud dissipation over land. This strong mixing is in stark contrast to the decoupling frequently observed in the STBL over the ocean.

Less research attention has been given to stratocumulus over land than over ocean, and of those studies, the majority have focused on postfrontal continental stratocumulus clouds (Kollias and Albrecht 2000; Zhu et al. 2001; Ghate et al. 2010; Fang et al. 2014a,b; Mechem et al. 2010a; Mechem et al. 2010b). Stratocumulus clouds over coastal land differ from clouds in the continental interior in two major ways. First, coastal stratocumulus clouds usually form in the summer when there is a strong inversion capping the STBL, whereas continental clouds often occur during the cool season when downwelling solar radiation is smaller (Mechem et al. 2010a). Second, horizontal advection by the sea breeze plays an important role in modulating coastal stratocumulus clouds. The transport of air from and to the ocean and the diurnal cycle of the surface energy budget are important in addition to shear and entrainment of free tropospheric air into the cloud layer (Sandu et al. 2010). An accurate assessment of coastal stratocumulus cloud evolution can only be made if all of these factors are considered.

In this paper, we use large-eddy simulation (LES) and a mixed layer model (MLM) to examine how cloud-top entrainment, surface Bowen ratio, and advection by the sea breeze contribute to cloud breakup during the morning transition of stratocumulus over coastal land. We will first use LES of some idealized cases to obtain a reference state of the cloud evolution that reasonably portrays the breakup of coastal stratocumulus clouds (section 3). Next, we describe modifications to the MLM to more accurately represent how changes in cloud-base and cloud-top temperature affect longwave radiation and to more accurately represent the combined effect of surface and cloud-driven buoyancy on turbulence and entrainment (section 4). Finally, the MLM is applied in conjunction with the LES to understand how STBL turbulence, entrainment, cloud liquid water path (LWP), and cloud thickness respond to the varying initial profiles, wet and dry land surfaces, large-scale advection, and subsidence (section 5).

2. Characterization of coastal stratocumulus

Over midlatitude coastal land areas, stratocumulus clouds usually form at night owing to the advection of cool ocean air onto the coast. They are especially prevalent during the summer months in the Northern Hemisphere owing to strong climatological anticyclones over the adjacent ocean. Using normalized global horizontal irradiance (GHI) observations [percentage of instantaneous clear-sky irradiance computed based on Ineichen and Perez (2002)] from a Li-200SZ (LiCor, Nebraska) pyranometer at the University of California, San Diego, we observe that the averaged irradiance is lowest during mornings in the months of May–September, compared to the rest of the year, corresponding with the occurrence of coastal stratocumulus clouds (Fig. 1a). Clouds begin to dissipate farthest inland first in the morning and at progressively later times closer to the coast, where the clouds often survive into the afternoon (Fig. 1b; Skupniewicz et al. 1991). Schwartz et al. (2014) analyzed six decades of airport observations to find that during the summer months low clouds, including stratocumulus clouds, respond to large-scale forcings, such as Pacific decadal oscillation, coherently across the entire west coast of North America and across a wide range of time scales.

Similar to the stratocumulus clouds occurring over the ocean, stratocumulus clouds over coastal land attain maximum coverage at sunrise. After sunrise, solar radiation warms the atmospheric STBL and land surface. Because of the lower heat capacity of land, a significant portion of the solar radiation absorbed at the surface is converted to convective surface fluxes, which in turn warm and moisten the STBL depending on land surface

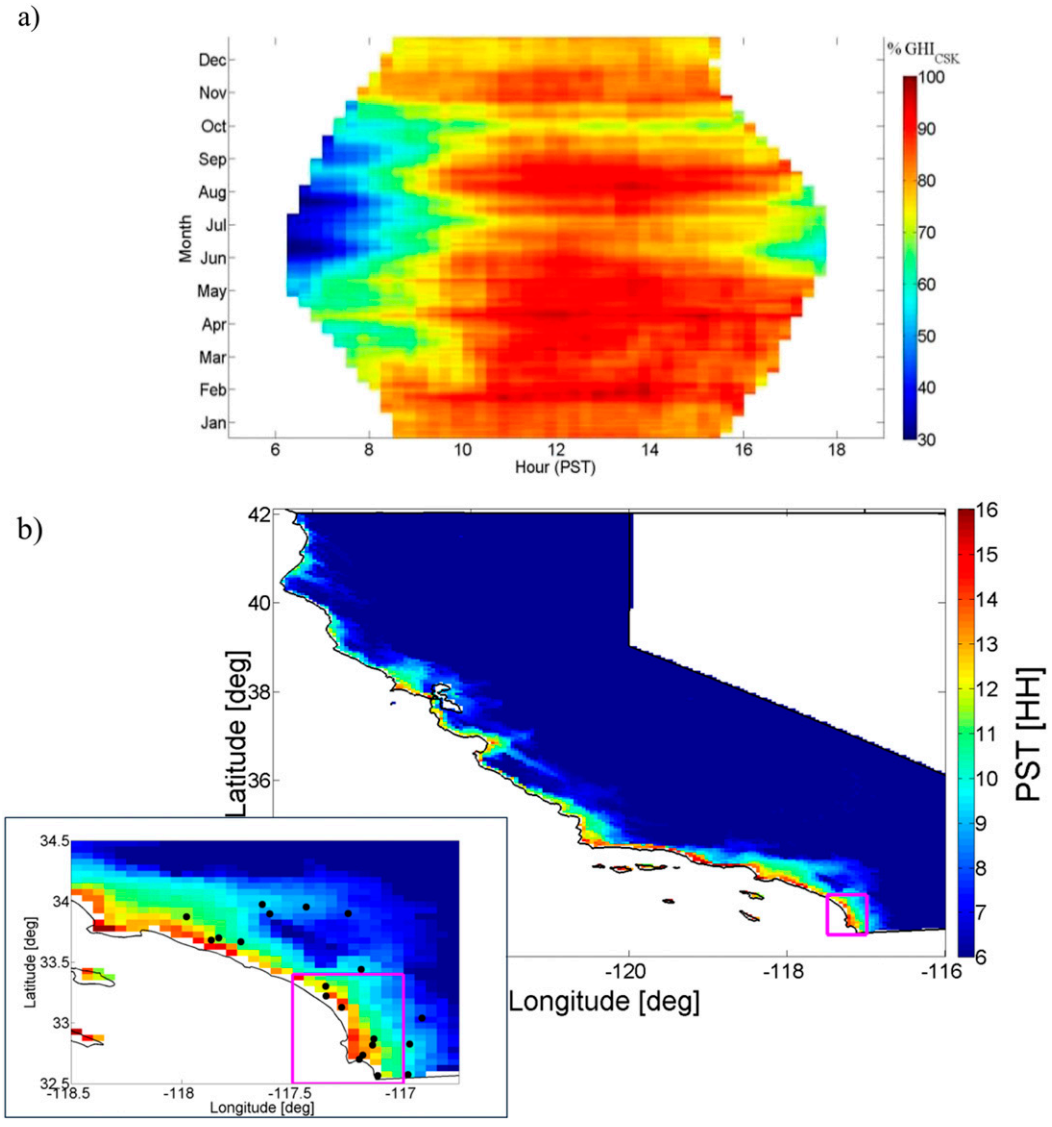

FIG. 1. (a) Normalized GHI observations measured using a pyranometer at the University of California, San Diego (32.88°N, 117.23°W, approximately 1 km from the Pacific Ocean) in 2011. (b) Averaged cloud dissipation time derived from satellite solar resource data for 2–9 Jun 2014 (SolarAnywhere 2014) for the state of California and averaged cloud dissipation time for southern California overlaid with METAR stations along the coast. The magenta box represents the domain where METAR wind data are acquired to model advection (32.5–33.3°N, 117°–118°W).

properties such as soil moisture content. Even though the Bowen ratio can be greater than one over land, the larger total available energy can result in a higher latent heat flux over land then over ocean. The surface buoyancy fluxes also drive turbulence in the STBL, which in turn increases the cloud-top entrainment and inversion height. Greater warming of land during day drives a stronger pressure difference between land and ocean boundary layers, which in turn increases onshore advection. The horizontal advection of marine air has a cooling effect on the land STBL and may decrease the absolute humidity over land even though the relative humidity of the advected marine air is higher than that of the onshore air. As the day progresses, surface flux heating/moistening, advection of cool oceanic air, and entrainment of warm dry air into the STBL all increase. Price (1999) studied the breakup of stratocumulus over the coast in the United Kingdom and found that cloud breakup was caused by solar heating in one case and by a combination of solar heating and shear-driven entrainment in another case.

While in reality the inland penetration of the stratocumulus clouds is limited by distance from the coast and

by topography, for the purpose of this paper we shall neglect topographical effects. We define three domains: an "over the ocean" domain, a "coupled" domain that consists of an STBL over the land with large-scale advection of cool moist air from the ocean, and a "land" domain that we assume to be sufficiently inland that advection does not play a significant role in modulating the cloud lifetime (Fig. 2). We simulate the ocean case to serve as a baseline analysis to compare against published results as well as to contrast against the coupled and land cases. The coupled case is chosen to study the effects of large-scale horizontal advection on cloud lifetime. Each of the coupled and land domains are further broken down into two cases: one consisting of a STBL over a wet land surface and another case over a moderately dry land surface. The wet and dry surface cases are chosen to study the effects of idealized surface moisture content and vegetation cover on cloud lifetime. Finally, we simulate the cases outlined above for two different initial thermodynamic profiles in order to test how initial STBL depth and inversion strength affect cloud lifetime together with testing how well the proposed MLM performs under different initial conditions.

3. Large-eddy simulations

a. Initial profiles and domain setup

We employ the University of California, Los Angeles (UCLA) LES model for the large-eddy simulations (Stevens et al. 2005; Savic-Jovcic and Stevens 2008). A cloud interactive radiation scheme based on Monte Carlo sampling of the spectral integration in the delta four stream radiation method was coupled with the LES in order to supply the radiative tendencies (Pincus and Stevens 2009). There has been a significant discussion in the literature on how to accurately model cloud-top entrainment velocity and the effects of entrainment flux on the STBL (e.g., Yamaguchi and Randall 2008; Mellado 2010; Stevens 2002). LES is restricted in its representation of entrainment by the vertical resolution, which is on the order of meters, in addition to its limited ability in tracking the cloud-top mixing interface and modeling the mixing (Stevens 2010). Despite these limitations, LES results were found to match those of measurements well for ocean cases (Stevens et al. 2005; Ackerman et al. 2009).

We simulate the CFMIP-GEWEX Global Atmospheric System (GASS) Intercomparison of LES and Single-Column Model (SCM; CGILS) S12 profile and the Dynamics and Chemistry of Marine Stratocumulus (DYCOMS) first research flight (RF01) profiles as they are representative of a well-mixed STBL (Fig. 3) and have been extensively reported on in the literature, including as initializations for LES intercomparisons (Stevens et al. 2003, 2005; Zhang et al. 2012; Blossey et al. 2013). Bretherton et al. (2013) ran LES and MLM initialized using the CGILS S12 profile to study the ocean STBL response to a variety of factors such as inversion strength, CO_2 concentration, and free tropospheric relative humidity. Both the CGILS S12 and DYCOMS RF01 profiles were developed for over-the-ocean model intercomparison studies; however, we do not anticipate any major differences in STBL profiles between land and ocean cases at night. While a weak temperature inversion may occur near the land surface due longwave cooling, the surface longwave cooling effect is greatly diminished in the presence of the cloud layer. There are two main deviations between real observations and CGILS S12 and DYCOMS profiles: 1) variations in liquid potential temperature $\theta_l(z)$ and total water mixing ratio $q_T(z)$ within the STBL and 2) thicker inversions. We find that LES based on sounding data with significant inversion thickness (but the same inversion strength) exhibits a qualitatively similar evolution of the cloud layer as the CGILS S12 results (not shown). We therefore expect that the LES and MLM simulations based on the CGILS and DYCOMS cases increase our understanding of the processes behind the cloud dissipation in more realistic situations, similar to how the idealized MLM of stratocumulus by Nicholls (1984) generated insight in more realistic marine cloud layers.

We follow the numerical setup of the CGILS LES intercomparison study: the vertical grid spacing is 10 m near the surface and refined (10% per layer) to obtain a 5-m resolution near the inversion, after which the grid is stretched again. The horizontal resolution is 25 m and the domain size is 2.4 km $\times$ 2.4 km in the horizontal and 1.6 km in the vertical (Blossey et al. 2013). In the CGILS S12 LES intercomparison study, the different LES were run to equilibrium conditions over 10 days with an interactive radiation scheme, diurnally averaged (constant) solar radiation, and varying sea surface temperature (Blossey et al. 2013). Little or no precipitation was reported for the duration of the 10-day runs. Thus, we do not consider precipitation and employ a simplified microphysics scheme that consists of a simple pure condensation scheme with no rain. We note that despite drizzle not being observed in the CGILS S12 case, drizzle is often observed in subtropical stratocumulus clouds (Leon et al. 2008). Moreover, unlike the CGILS LES intercomparison, we allow solar position to undergo a diurnal cycle over the 24-h simulation starting at 0000 LST. Large-scale mean subsidence is assumed to be steady since it typically does not vary significantly over 24 h. The LES exhibit a characteristic "spinup" period during the first 2 h (0000–0200 LST), during which turbulent eddies develop as a result of unstable conditions in the STBL due to cloud-top longwave cooling.

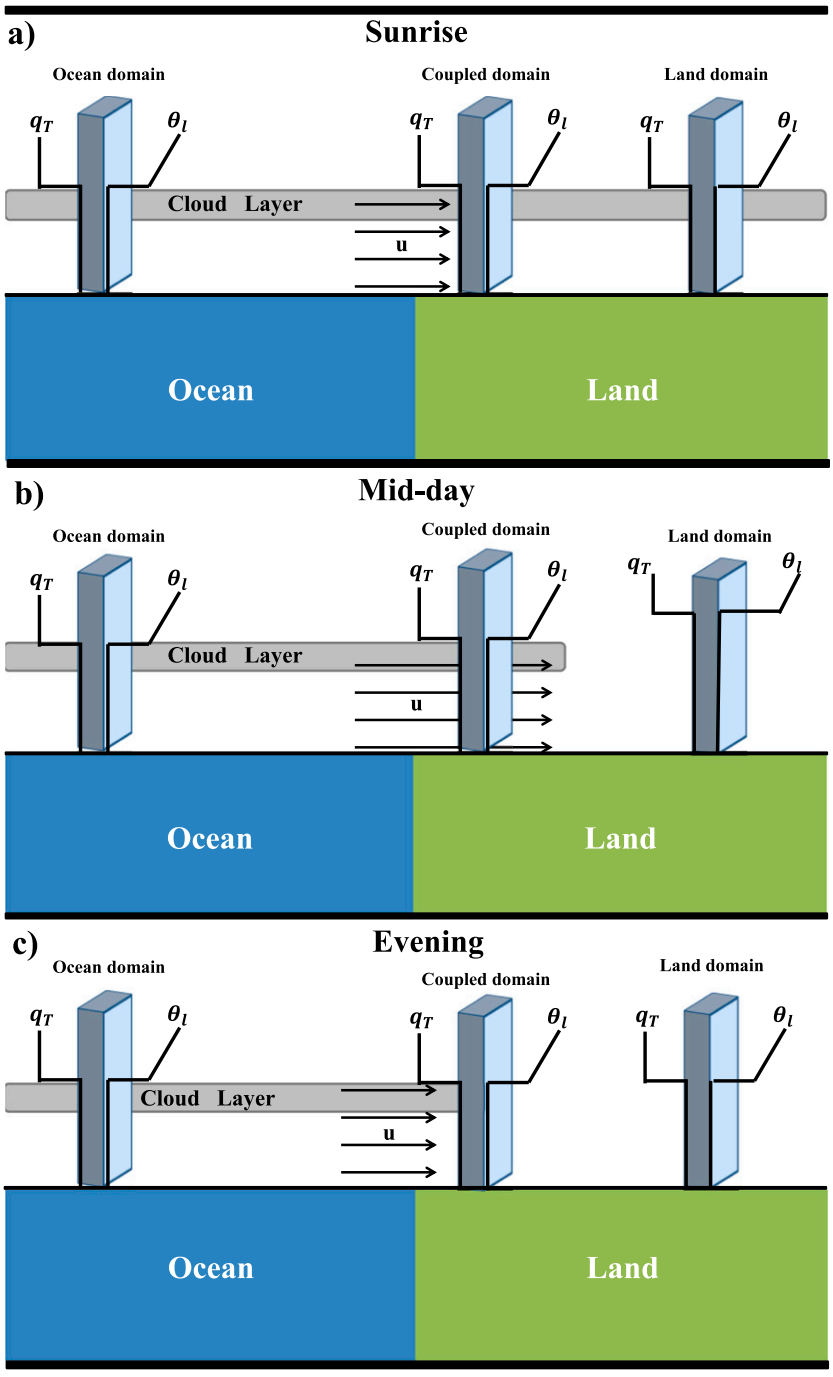

FIG. 2. Schematic description of stratocumulus cloud dissipation. (a) At sunrise, the stratocumulus cloud extends from over the ocean inland, thermodynamic profiles are well mixed, and there is a strong thin inversion. (b) At midday, the stratocumulus cloud begins breaking up inland first and the dissipation propagates toward the coast. The cloud has dissipated inland, giving rise to a clear dry convective boundary layer. Near the coast the cloud has thinned significantly and is near dissipation. Over the ocean the cloud has thinned but less so owing to lower surface warming occurring in the ocean domain. For all three domains the boundary layer remains well mixed driven by longwave cooling in the ocean surface case and surface flux in the land cases. (c) In the evening, the horizontal extent of the stratocumulus is at its minimum. The clear dry convective boundary layer inland begins to collapse as the surface flux driving turbulence decreases. Near the coast, the cloud has dissipated but the inversion is supported by the advection of oceanic air mass inland. Over the ocean, the cloud begins to thicken as solar radiation goes to zero. During the night as the cloud thickens over the ocean it is advected inland.

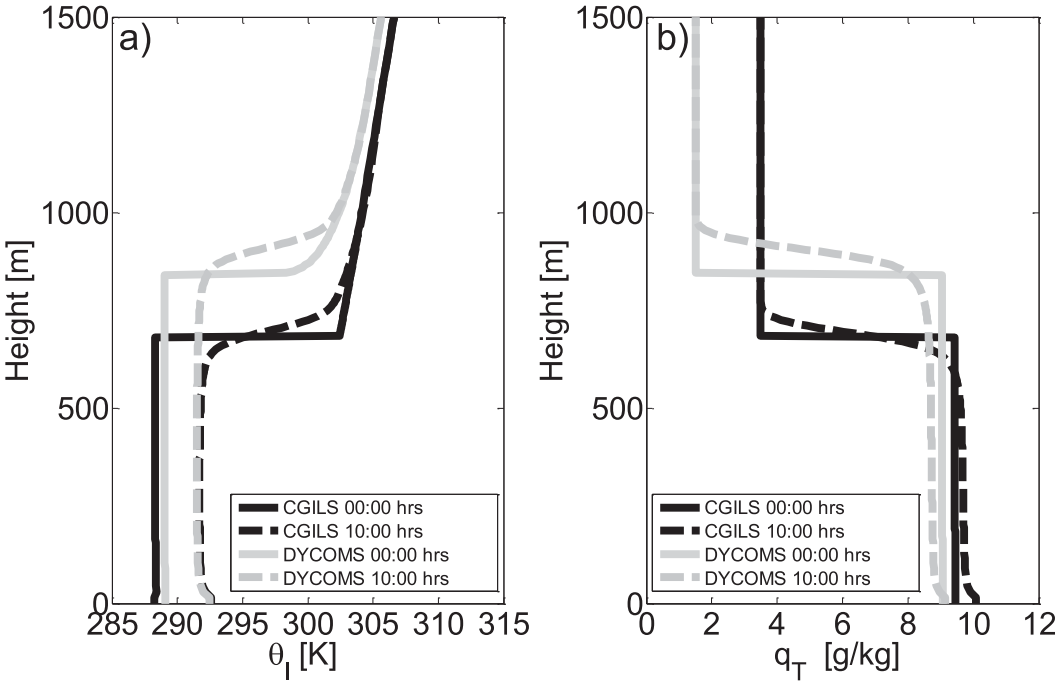

FIG. 3. (a) Liquid potential temperature and (b) total water mixing ratio for CGILS S12 (black lines) and DYCOMS (gray lines) simulations at the start of the simulation (0000 LST, solid line) and at 1000 LST for the 1.0 Bowen ratio land case (dashed line).

We carry out LES initialized with both the CGILS and the DYCOMS profiles for five cases. The first three are for STBLs (i) over the ocean, (ii) over a wet land surface, and (iii) over a moderately dry land surface. The next two are ''coupled'' cases that include advection from ocean to land for (iv) a wet land surface and (v) a moderately dry land surface.

b. *Surface fluxes*

For the ocean cases we follow the CGILS LES intercomparison study and employ a simplified surface flux formula as

$$\mathrm{SHF} = C_T(\mathrm{SST} - \theta_{l1}) \quad \text{and} \tag{1a}$$

$$\mathrm{LHF} = C_T[0.98q_{\mathrm{sat}}(P_s, \mathrm{SST}) - q_{T1}], \tag{1b}$$

where θ_{l1} and q_{T1} are liquid potential temperature and total water mixing ratio at the lowest model fluid level, respectively. The variable $q_{\mathrm{sat}}(P_s, \mathrm{SST})$ is the saturation specific humidity at the surface pressure (P_s) and sea surface temperature (SST). The transfer coefficient term C_T is calculated as a function of the surface wind velocity (Blossey et al. 2013).

For the land cases, the convective fluxes are larger and the partitioning of available energy into sensible (SHF) and latent heat fluxes (LHF), described by the Bowen Ratio (β = SHF/LHF), is of primary importance for stratocumulus lifetime. We assume a constant Bowen ratio for simplicity rather than employ a detailed land surface model that lacks generality and introduces many empirical parameters. Although the similarity of exchange coefficients for heat and water and the longer time scale for changes in soil moisture content compared to atmospheric turbulence motivate the use of a constant Bowen ratio, several limitations exist in practice. For large available energy at the surface, the ability of the vegetation to conduct sufficient water to the surface to maintain the Bowen ratio may be limited by stomatal conductance or leaf area; this results in increasing Bowen ratio as the morning progresses during clear days. However, this limitation is largely irrelevant for the cases studied in this paper since stratocumulus clouds attenuate the solar energy at the surface. The Bowen ratio will also vary if surface air is near saturation and inhibits latent heat flux or if the soil moisture in the root zone or top soil layer reaches the permanent wilting point, but neither is the case in our simulations. Typical Bowen ratio values range from 0.1 over irrigated orchards to 0.2 over forests and grasslands to 2 for urban and semiarid regions (EPA 2004). We chose a Bowen ratio of 0.1 to represent the wet surface case and a Bowen ratio of 1.0 to represent the moderately dry surface case.

In both the LES and the MLM, the convective surface fluxes were parameterized as a function of the net surface radiation and Bowen ratio as

$$\mathrm{SHF} = \phi\left(\frac{\beta}{\beta+1}\right)F_{\mathrm{rad0}} \quad \text{and} \tag{2a}$$

$$\mathrm{LHF} = \phi\left(\frac{1}{\beta+1}\right)F_{\mathrm{rad0}}, \tag{2b}$$

where ϕ is the efficiency at which net surface radiation (F_{rad0}) is converted to convective surface fluxes. The latent heat flux LHF is set to zero at night as dew formation is negligible in cloud-topped BLs. The surface energy balance equation is then formulated as

$$F_{\mathrm{rad0}} = \phi\left(\frac{\beta}{\beta+1}\right)F_{\mathrm{rad0}} + \phi\left(\frac{1}{\beta+1}\right)F_{\mathrm{rad0}} + (1-\phi)\left[\varphi c_p\frac{dT_{\mathrm{srf}}}{dt} + (1-\varphi)G\right], \tag{3}$$

where T_{srf} is the surface temperature, G represents the ground heat flux, and φ partitions the heat input into the soil between the top layer $[c_p(dT_{\mathrm{srf}}/dt)]$ and the lower layers (G).

The parameterized surface fluxes were tested against a more sophisticated land surface model (LSM) described in Heus et al. (2010) and Rieck et al. (2014), where the coupling to the LES is also described in more detail. The parameterized surface fluxes in Eqs. (2) and (3) were found to be in good agreement with the surface flux of the LSM. Furthermore, both ϕ and φ were found to be relatively constant throughout the daytime and equal to 0.9 and 0.04, respectively.

c. *Large-scale advection*

Due to the limited horizontal extent of the LES, we are unable to simulate mesoscale atmospheric processes and explicitly compute advective tendencies for the case with ocean–land interaction. Meteorological observations are also not sufficient to compute advection as continuously operating, horizontally displaced profiles would be required. As an alternative, we introduce a simple model to apply large-scale horizontal forcings ($\overline{\boldsymbol{v}}\cdot\nabla_h\overline{\theta_l}$, $\overline{\boldsymbol{v}}\cdot\nabla_h\overline{q_T}$) to the LES as follows:

$$\overline{\boldsymbol{v}}\cdot\nabla_h\overline{\theta_l} = \overline{\boldsymbol{v}}\cdot[\overline{\theta}_{l\mathrm{land}}(z,t) - \overline{\theta}_{l\mathrm{ocean}}(z,t)]/\Delta x \quad \text{and} \tag{4a}$$

$$\overline{\boldsymbol{v}}\cdot\nabla_h\overline{q_T} = \overline{\boldsymbol{v}}\cdot[\overline{q_T}_{\mathrm{land}}(z,t) - \overline{q_T}_{\mathrm{ocean}}(z,t)]/\Delta x, \tag{4b}$$

where z represents the LES domain height and $\overline{\boldsymbol{v}}$ is the large-scale horizontal surface wind reported hourly from seven METAR stations (32.5–33.3°N, 117°–118°W) on the southern California coast for 2 June 2014 (Fig. 4a). This day was chosen because Geostationary Operational Environmental Satellite (GOES) imagery showed a typical stratocumulus day with widespread cloud cover at dawn and dissipation progressing from inland toward the ocean through the day (Fig. 1b). There are primarily westerly winds throughout the day (Fig. 4b), which is representative of summer months along the North American coast due to the North Pacific high and the ocean–land thermal gradient (Taylor et al. 2008).

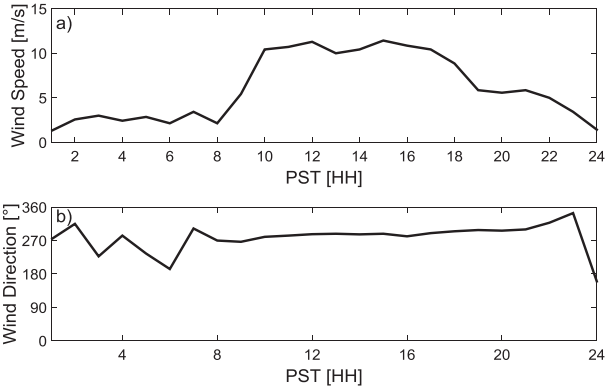

FIG. 4. Surface wind speed (a) magnitude and (b) direction collected from METAR stations along the coast of California (32.5–33.3°N, 117°–118°W; see Fig. 1b).

The LES ocean case provided values of liquid potential temperature and total water mixing ratio profiles $[\overline{\theta_l}_{\mathrm{ocean}}(z,t), \overline{q_T}_{\mathrm{ocean}}(z,t)]$ for use in Eqs. (4a) and (4b), while $\overline{\theta_l}_{\mathrm{land}}(z,t)$ and $\overline{q_T}_{\mathrm{land}}(z,t)$ were dynamically computed within the LES run. The length scale Δx is representative of the strength of the large-scale advective tendencies. As Δx increases, the large-scale advective tendencies decrease, corresponding to a domain farther inland and not significantly affected by the land–ocean temperature and moisture gradients. For the purpose of this study we chose $\Delta x = 30$ km, which is representative of the scale of inland penetration of stratocumulus. We note that this is an idealized analysis and that we made the following simplifying assumptions: (i) surface wind velocity measurements are representative of the boundary layer wind profiles, (ii) wind direction is perpendicular to the coast, and (iii) topographic effects are negligible. Although these assumptions lead to significant deviations from the actual advective tendencies, our goal is to gain a sense of how large-scale advection affects the cloud layer. Hence, we believe that our assumptions are reasonable within our idealized framework.

4. Mixed layer model

The MLM is a thermodynamic model that has been applied to various atmospheric boundary layers, including dry convective and the STBL over the ocean (Bretherton and Wyant 1997; Uchida et al. 2010; Dal Gesso et al. 2014). The MLM solves the STBL mass, heat, and moisture

budget equations (Lilly 1968; refer to our appendix A for an overview of the equations). Turbulence in the STBL is generated by either longwave radiative divergence across the cloud layer or by surface flux, and unstable conditions are assumed to prevail. Thus, the thermodynamic properties are assumed to follow adiabatic values, and the STBL is taken to be well mixed (Albrecht et al. 1990; Caldwell et al. 2005). The well-mixed assumption breaks down when the STBL becomes decoupled owing to a reduction in turbulence or an increase in the inversion height. We did not observe any significant deviations from the well-mixed assumption in this study since the inversions height does not exceed 1 km for the cases we have chosen. Furthermore, surface buoyancy flux in the land cases is a significant source of turbulence that keeps the STBL well mixed. While the MLM framework and budget equations are taken from the literature, to improve the MLM accuracy for STBL over land several parameterizations are modified or introduced in the following sections.

a. Radiation parameterization

An analytical radiation scheme that models longwave radiation (F_{LW}) as a function of the STBL LWP and temperature is coupled to the MLM. It is different from the radiation scheme employed in the LES since the latter is too computationally expensive to be coupled to the MLM. The radiation scheme in the MLM is similar to that used in the Global Energy and Water Cycle Experiment (GEWEX) Cloud System Study (GCSS; Bretherton et al. 1999), which was found to yield accurate fluxes for liquid clouds (Larson et al. 2007). However, the GEWEX radiation parameterization does not account for the cloud-base and cloud-top temperature changes that are crucial for the STBL occurring over land, where there is significant heating from the surface. Thus, we modified the radiation scheme to be a function of these temperatures in the MLM, and the resulting net longwave radiation can be expressed as

$$F_{\mathrm{LW}} = Le^{\alpha\tau} + Me^{-\alpha\tau} + \rho_{\mathrm{air},i}c_pD\alpha_Z\left[\frac{(z-z_i)^{4/3}}{4} + z_i(z-z_i)^{1/3}\right]. \quad (5)$$

Refer to appendix B for a more detailed derivation of the net longwave flux equation and definitions of the quantities appearing therein.

The net downward solar radiation (F_{SW}) is derived using the analytical solution of the delta–Eddington approximation (Joseph et al. 1976; Shettle and Weinman 1970; Duynkerke et al. 2004) and is expressed as

$$F_{\mathrm{SW}}(z) = \frac{4}{3}F_0\{p[A_1e^{-k\tau(z)} - A_2e^{k\tau(z)}] - \beta e^{-\tau(z)/\mu_0}\} + \mu_0F_0e^{-\tau(z)/\mu_0}, \quad (6)$$

where $\mu_0 = \cos\theta$, θ is the solar zenith angle, $F_0 = 1100\,\mathrm{W\,m^{-2}}$ is the downward solar radiation at the cloud top, constants A_1 and A_2 are computed based on the boundary conditions, p and β are functions of the asymmetry factor and single scattering albedo, and $\tau(z)$ is the optical depth and is defined as

$$\tau(z) = \frac{3}{2}\frac{\mathrm{LWP}}{r_e\rho_w}, \quad (7)$$

where r_e is the cloud droplet effective radius (i.e., the ratio of the third moment to the second moment of the droplet size distribution). For marine boundary layer clouds, we chose $r_e = 10\,\mu$m, which was observed for stratocumulus over the Pacific Ocean off the coast of California (Duda et al. 1991). Liquid water density is represented by ρ_w.

b. Entrainment parameterization

We assume that the STBL is a shear-free, convective boundary layer. Under that assumption, the main driver of turbulence in a STBL over ocean is cloud-top longwave radiative cooling (also see section 5). For a STBL over land, the main source of turbulence shifts from cloud-top longwave radiative cooling during night to surface generated buoyancy during day (refer to section 5). To parameterize entrainment velocity for both cases, we first formulate the total velocity scale as a linear combination of the buoyancy flux generated in the cloud layer due to the radiative divergence and the buoyancy flux generated at the surface as

$$w_T^{*3} = w_{\mathrm{rad}}^{*3} + w_{\mathrm{srf}}^{*3} = 2.5\frac{g}{\theta_{v0}}\int_{z_b}^{z_i}\overline{w'\theta_v'}\,dz + 1.25\frac{gz_i}{\theta_{v0}}\overline{w'\theta_{vs}'}, \quad (8)$$

where $\overline{w'\theta_{vs}'}$ is the virtual potential flux evaluated at the surface and θ_{v0} is the reference virtual potential temperature taken to be 290 K. Fang et al. (2014a) also formulated a total velocity scale as linear combination of the buoyancy flux generated at the surface and the radiative convective velocity. Utilizing ground measurements, Fang et al. (2014a) were able to show that the total convective velocity scale w_T^{*3} tracked the turbulence forcing well throughout the day. Furthermore, they found that turbulence at night is mainly driven by the cloud-top cooling characterized by w_r^{*3} whereas turbulence during the day is driven by both cloud-top cooling and surface flux. Rather than use net radiative flux divergence as did Fang et al. (2014a) $\{w_r^{*3} = [(gz_i)/(\rho c_p\theta_{v0})](-\Delta F_r)\}$, we

use the in-cloud buoyancy flux as a measure of the turbulence generated by the net longwave radiative flux divergence across the cloud layer as well as the turbulence generated by latent heat release in updrafts within the cloud layer. We hypothesize that the integral of the in-cloud buoyancy flux is a more appropriate velocity scale considering that cloud-top longwave emission becomes insensitive to LWP changes for thick clouds (Kazil et al. 2015). Thus, for sufficiently thick clouds, additional turbulence generation and boundary layer growth is produced by latent heat release in updrafts within the cloud layer rather than increased longwave emission.

Next, we parameterize the cloud-top entrainment velocity as

$$w_e = A\left(\frac{w^*_{\mathrm{rad}}}{\mathrm{Ri}_{\mathrm{rad}}} + \frac{w^*_{\mathrm{srf}}}{\mathrm{Ri}_{\mathrm{srf}}}\right), \tag{9}$$

where $\mathrm{Ri}_{\mathrm{rad}} = (gz_{\mathrm{cld}}\Delta\theta_{vi})/(\theta_{v0}w^{*2}_{\mathrm{rad}})$ and $\mathrm{Ri}_{\mathrm{srf}} = (gz_i\Delta\theta_{vi})/(\theta_{v0}w^{*3}_{\mathrm{srf}})$ are the bulk Richardson numbers for the radiative-driven turbulence and surface-driven turbulence, respectively. The variable z_{cld} represents the cloud thickness and a floor of $z_{\mathrm{cld}} = 0.1 \times z_i$ is set for when the cloud dissipates. Cloud thickness is defined as the difference between the inversion height and the cloud-base height, defined as the height corresponding to the maximum liquid potential temperature gradient and the minimum height at which the liquid water mixing ratio is greater than zero, respectively. In the Richardson numbers $\Delta\theta_{vi}$ is the inversion jump in virtual potential temperature. The variable A represents the entrainment efficiency and is expressed as

$$A = a_1\left[1 + a_2\left(1 - \frac{\Delta_m b}{\Delta_i b}\right)\right], \tag{10}$$

where the term a_2 $[1 - (\Delta_m b)/(\Delta_i b)]$ accounts for the evaporative enhancement of entrainment, and $\Delta_m b$ is the linearized average buoyancy of all possible mixtures between purely clear tropospheric air and purely cloudy air, relative to the cloudy air [refer to appendix B of Grenier and Bretherton (2001) for a detailed derivation and description of Eq. (10)]. The buoyancy jump across the inversion is represented by $\Delta_i b$ and the values $a_1 = 0.2$ and $a_2 = 60$ are based on fits to observations and laboratory experiments (Nicholls and Turton 1986). As the cloud begins to dissipate, the evaporative enhancement goes to 0 and A goes to 0.2, which is the entrainment efficiency for a dry mixed layer. Thus, the entrainment parameterization we propose is a linear combination of two regimes: the first occurs at night and is driven by longwave cooling with turbulence mainly concentrated in the cloud layer; the second occurs at day and is driven by surface heating with turbulence that is almost an order of magnitude stronger and encompasses the entire boundary layer.

Next, in order to solve for the in-cloud virtual potential temperature flux we equate it to the conserved variable fluxes as follows:

$$\overline{w'\theta'_v}(z) = C_1\overline{w'\theta'_l}(z) + C_2\overline{w'q'_T}(z), \quad z_b < z < z_i, \tag{11}$$

where $C_1 = \{[1 + (\overline{q_s}/\epsilon) - \overline{q_T} + (\overline{\theta}/\epsilon)(dq_s/dT)]/[1 + (L_v/c_p)(dq_s/dT)]\} \approx 0.5$ and $C_2 = (L_v/c_p)\{[1 + (\overline{q_s}/\epsilon) - \overline{q_T} + (\overline{\theta}/\epsilon)(dq_s/dT)]/[1 + (L_v/c_p)(dq_s/dT)]\} - \overline{\theta} \approx 970\,\mathrm{K}$ [refer to Stevens (2002) for a more detailed derivation of the constants]. In order for the STBL to remain well mixed, $(\partial\overline{\theta_l}_{\mathrm{BL}}/\partial t) + (\overline{\boldsymbol{v}}\cdot\nabla_h\overline{\theta_l})_{\mathrm{BL}}$ and $(\partial\overline{q_T}_{\mathrm{BL}}/\partial t) + (\overline{\boldsymbol{v}}\cdot\nabla_h\overline{q_T})_{\mathrm{BL}}$ must be height independent. To satisfy Eqs. (A2) and (A3), $\overline{w'\theta'_l}(z) + [F_{\mathrm{rad}}(z)/(c_p\rho_{\mathrm{air}})]$ and $\overline{w'q'_T}(z)$ must therefore be linear functions of height in the STBL and can be expressed as follows:

$$\overline{w'\theta'_l}(z) + \frac{F_{\mathrm{rad}}(z)}{c_p\rho_{\mathrm{air}}} = \left(1 - \frac{z}{z_i}\right)\frac{\mathrm{SHF} + F_{\mathrm{LW0}}}{\rho c_p} - \frac{z}{z_i}\left(w_e\Delta\theta_{li} - \frac{F_{\mathrm{LW}i}}{\rho c_p}\right) \quad \text{and} \tag{12}$$

$$\overline{w'q'_T} = \left(1 - \frac{z}{z_i}\right)\frac{\mathrm{LHF}}{\rho L_v} - \frac{z}{z_i}w_e\Delta q_{Ti}. \tag{13}$$

To define the jumps in heat and moisture across the inversion ($\Delta\theta_{li}$, $\Delta\theta_{vi}$, and Δq_{Ti}), we must determine the thickness of the entrainment zone (also referred to as the inversion layer or interfacial layer; Fig. 3). The entrainment zone is the region where air from the overlying free atmosphere is entrained across the inversion into the convectively mixed STBL. The entrainment is fed by the penetration of thermals from the STBL into the stably stratified air above the inversion that cause the descent of more buoyant air aloft into the STBL.

The thickness of the entrainment zone is an active research topic. Studies conducted by Sullivan et al. (1998) and Fedorovich et al. (2004) on clear convectively driven boundary layers considered a single layer to exist within the entrainment zone. More recently, Garcia and Mellado (2014) showed that the entrainment zone consists of two overlapping sublayers: an upper sublayer that is dominated by thermals and stratification and a lower layer dominated by troughs (crests of undulations within the entrainment zone at the cloud top) of mixed fluid. In the case of the STBL over land, defining the entrainment zone is further complicated by an inversion that is rapidly weakening as a result of surface heating and rising in height because of increased encroachment fed by the enhanced turbulence resulting from the land surface flux

(Figs. 5d–i and 6c–f). Because of the uncertainties regarding the definition of entrainment zone heights and insufficient resolution in LES to accurately represent the physical processes occurring in the entrainment zone, we utilize the entrainment zone thickness as a tuning parameter to match LES derived entrainment velocity with that of the MLM. Thus, we set two different entrainment zone heights: one for the cloud-top radiative cooling contribution and another for the surface flux contribution, equal to 3.4 and 7.5 m, respectively. The entrainment zone heights remain constant throughout the simulation and do not change between cases.

c. Factors contributing to cloud dissipation

To study how different physical processes such as entrainment and radiation divergence affect cloud lifetime, the MLM equations [Eqs. (A1)–(A3)] are coupled with the cloud thickness ($z_{\rm cld}$) tendency equation. Following Ghonima et al. (2015), the cloud thickness tendency is formulated as

$$\frac{\partial z_{\rm cld}}{\partial t} = \frac{\partial z_i}{\partial t} - \frac{c_p \Pi_{b,1}}{g}\left(1 - \frac{c_p R_v T_{b,1}}{R_d L_v}\right)^{-1} \frac{\partial \theta_L}{\partial t} - \frac{R_d T_{b,1}}{g q_T}\left(1 - \frac{L_v R_d}{c_p R_v T_{b,1}}\right)^{-1} \frac{\partial q_T}{\partial t}, \tag{14}$$

where $T_{b,1}$ is the cloud-base temperature and $\Pi_{b,1} = (P_{b,1}/P_0)^{R_d/C_p}$ is the Exner function. Substituting the inversion height and conserved variable tendencies [Eqs. (1)–(3)] into Eq. (14),

$$\begin{aligned}\frac{\partial z_{\rm cld}}{\partial t} = {} & w_e + w_s(z_i) - \boldsymbol{v}_H \cdot \nabla z_i \\ & - \frac{c_p \Pi_{b,1}}{z_i g}\left(1 - \frac{c_p R_v T_{b,1}}{R_d L_v}\right)^{-1}\left[-z_i(\overline{\boldsymbol{v}} \cdot \nabla_h \overline{\theta_l})_{\rm BL} + \overline{w'\theta'_{l0}} + w_e \Delta\theta_{li} - \frac{\Delta F_{\rm rad}}{c_p \rho_{\rm air}}\right] \\ & - \frac{R_d T_{b,1}}{z_i g q_T}\left(1 - \frac{L_v R_d}{c_p R_v T_{b,1}}\right)^{-1}\left[-z_i(\overline{\boldsymbol{v}} \cdot \nabla_h \overline{q_T})_{\rm BL} + \overline{w'q'_{T0}} + w_e \Delta q_{Ti}\right].\end{aligned} \tag{15}$$

We then split Eq. (15) into the five different physical factors contributing to the cloud thickness tendency as

$$\text{Entrainment flux} = w_e - \frac{c_p \Pi_{b,1}}{z_i g}\left(1 - \frac{c_p R_v T_{b,1}}{R_d L_v}\right)^{-1} w_e \Delta\theta_{li} - \frac{R_d T_{b,1}}{z_i g q_T}\left(1 - \frac{L_v R_d}{c_p R_v T_{b,1}}\right)^{-1} w_e \Delta q_{Ti}, \tag{16a}$$

$$\text{Surface flux} = -\frac{c_p \Pi_{b,1}}{z_i g}\left(1 - \frac{c_p R_v T_{b,1}}{R_d L_v}\right)^{-1} \overline{w'\theta'_{l0}} - \frac{R_d T_{b,1}}{z_i g q_T}\left(1 - \frac{L_v R_d}{c_p R_v T_{b,1}}\right)^{-1} \overline{w'q'_{T0}}, \tag{16b}$$

$$\text{Radiation} = \frac{c_p \Pi_{b,1}}{z_i g}\left(1 - \frac{c_p R_v T_{b,1}}{R_d L_v}\right)^{-1} \frac{\Delta F_{\rm rad}}{c_p \rho_{\rm air}}, \tag{16c}$$

$$\text{Subsidence} = w_s(z_i), \quad \text{and} \tag{16d}$$

$$\begin{aligned}\text{Advection} = {} & -\boldsymbol{v}_H \cdot \nabla z_i + \frac{c_p \Pi_{b,1}}{g}\left(1 - \frac{c_p R_v T_{b,1}}{R_d L_v}\right)^{-1} (\overline{\boldsymbol{v}} \cdot \nabla_h \overline{\theta_l})_{\rm BL} \\ & + \frac{R_d T_{b,1}}{g q_T}\left(1 - \frac{L_v R_d}{c_p R_v T_{b,1}}\right)^{-1} (\overline{\boldsymbol{v}} \cdot \nabla_h \overline{q_T})_{\rm BL}.\end{aligned} \tag{16e}$$

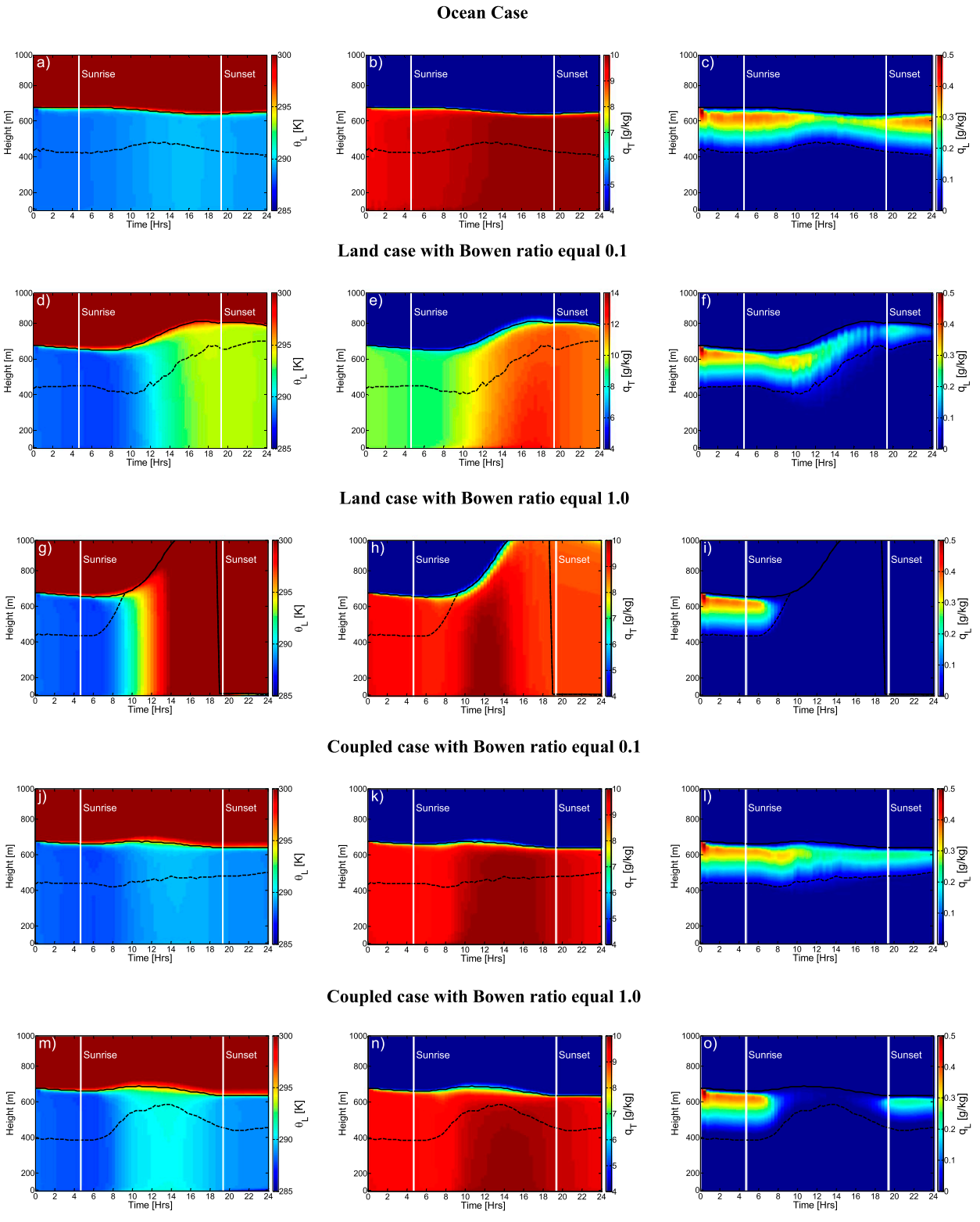

FIG. 5. Horizontally averaged temporal evolutions from LES of vertical profiles for the CGILS case of (a),(d),(g),(j),(m) liquid potential temperature ($\overline{\theta_l}$), (b),(e),(h),(k),(n) total water mixing ratio ($\overline{q_T}$), and (c),(f),(i),(l),(o) liquid water mixing ratio ($\overline{q_l}$). Results are provided for (a)–(c) the ocean case, (d)–(f) land case with Bowen ratio equal 0.1, (g)–(i) land case with Bowen ratio equal 1.0, (j)–(l) coupled case with horizontal advection representing the diurnally varying sea breeze circulation and Bowen ratio equal to 0.1, and (m)–(o) coupled case with horizontal advection representing the diurnally varying sea breeze circulation and Bowen ratio equal to 1.0. While the LES domain reaches up to 1.6 km, only the lowest kilometer is shown to focus on the boundary layer dynamics.

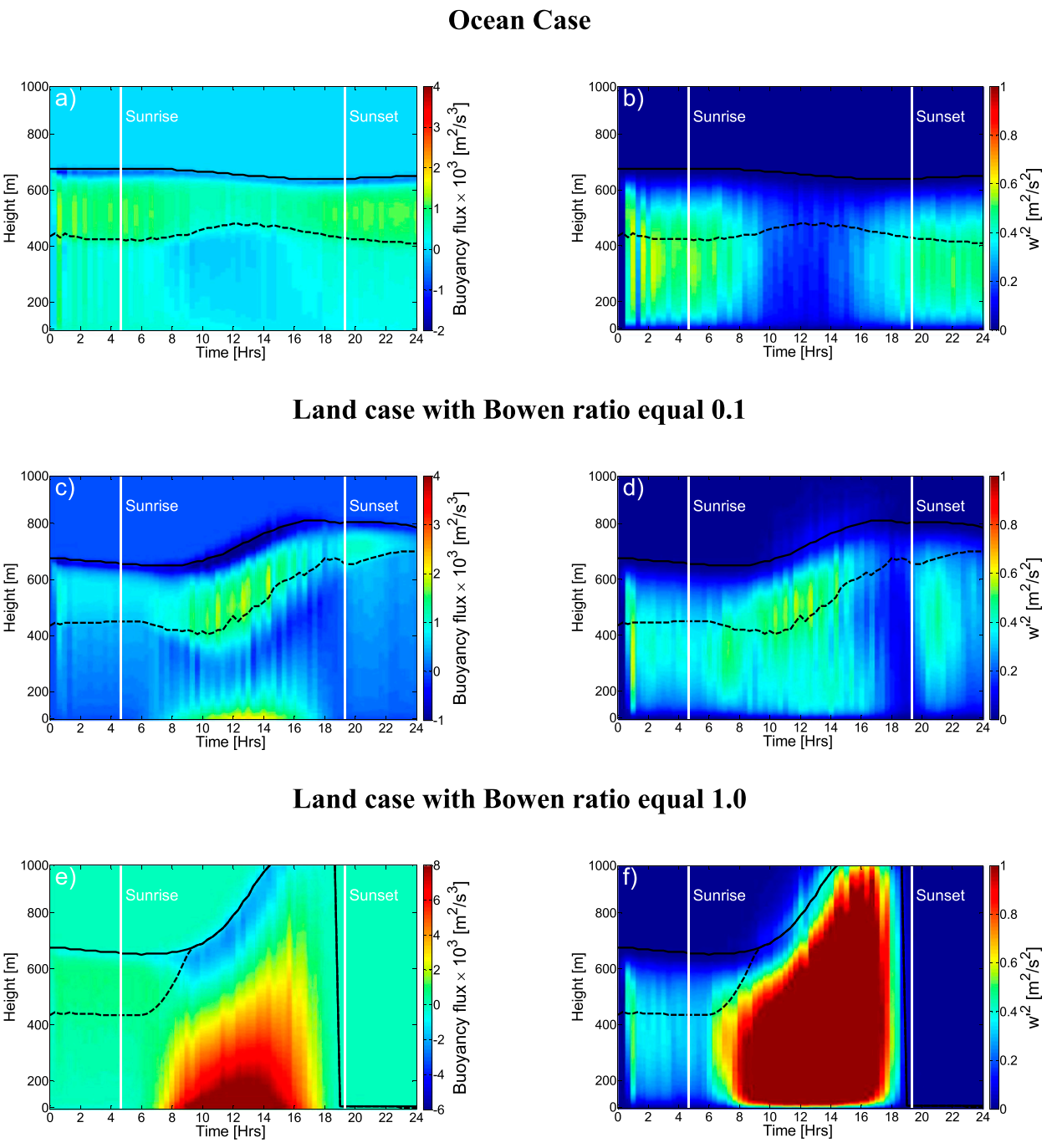

FIG. 6. Horizontally averaged temporal evolutions from LES for the CGILS case of vertical profiles of (a),(c),(e),(g),(i) buoyancy flux, and (b),(d),(f),(h),(j) vertical velocity variance ($\overline{w'^2}$). Results are shown for (a),(b) the ocean case, (c),(d) land case with Bowen ratio equal 0.1, (e),(f) land case with Bowen ratio equal 1.0, (g),(h) coupled case with horizontal advection representing the diurnally varying sea breeze circulation and Bowen ratio equal to 0.1, and (i),(j) coupled case with horizontal advection representing the diurnally varying sea breeze circulation and Bowen ratio equal to 1.0. While the LES domain reaches up to 1.6 km, only the lowest kilometer is shown to focus on the boundary layer dynamics.

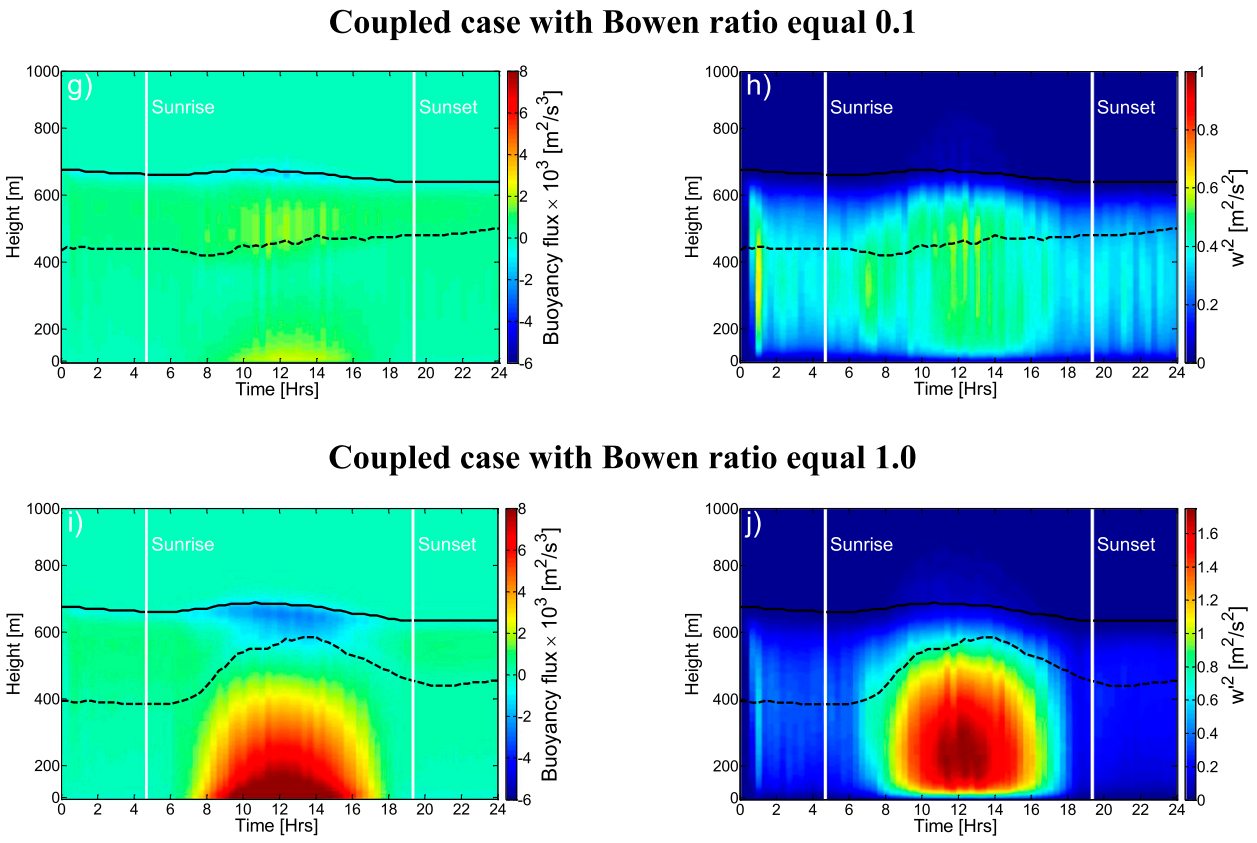

FIG. 6. (*Continued*)

5. Results and discussion

We present LES and MLM results for five cases: (i) ocean case, (ii) relatively wet land surface case (β = 0.1), (iii) moderately dry land surface case (β = 1.0), (iv) relatively wet land surface case (β = 0.1) "coupled" to the ocean STBL by horizontal advection, and (v) moderately dry surface case (β = 1.0) "coupled" to the ocean STBL by horizontal advection. The analysis is performed using both the CGILS and DYCOMS initial profiles. In the noncoupled cases (i, ii, and iii), we assume that horizontal heterogeneity is negligible and that the large-scale horizontal advection of heat and moisture does not affect either domain. Conversely, the coupled cases are motivated by actual coastal conditions where temperature and moisture gradients are significant and large-scale advection plays an important role in modulating the cloud lifetime. For each of the cases outlined, we compare the MLM output against the LES results up to the time of cloud dissipation since we are interested in studying the factors affecting cloud lifetime. We apply Eq. (16) to the MLM output in order to understand how each physical process contributes to the cloud thickness tendency.

a. Ocean case—Baseline analysis

The ocean results confirm well-known stratocumulus behavior (Figs. 5a–c). LWP varies diurnally over the ocean with maximum LWP occurring just before sunrise. LWP decreases after sunrise owing to solar radiative heating across the cloud layer that warms the boundary layer, causing cloud evaporation. Minimum LWP occurs at 1340 LST and at a value of 31 g m^{-2}. The solar radiative heating additionally reduces the buoyancy flux (Fig. 6a) generated through longwave radiative cooling within the cloud layer and correspondingly reduces the turbulence within the STBL (reduction in vertical velocity variance; Fig. 6b). Thus, in addition to directly heating the STBL, solar radiative forcing indirectly affects LWP by reducing buoyancy flux generated within the cloud layer and thus entrainment of warm and dry air into the STBL.

The MLM and LES results are in good agreement (Fig. 7). In all LES cases, there is a drop in LWP during 0000–0200 LST possibly because of spinup effects; consequently, LWP in LES is slightly lower than that of the MLM. The MLM results better match those of the LES when the MLM was initiated with LES

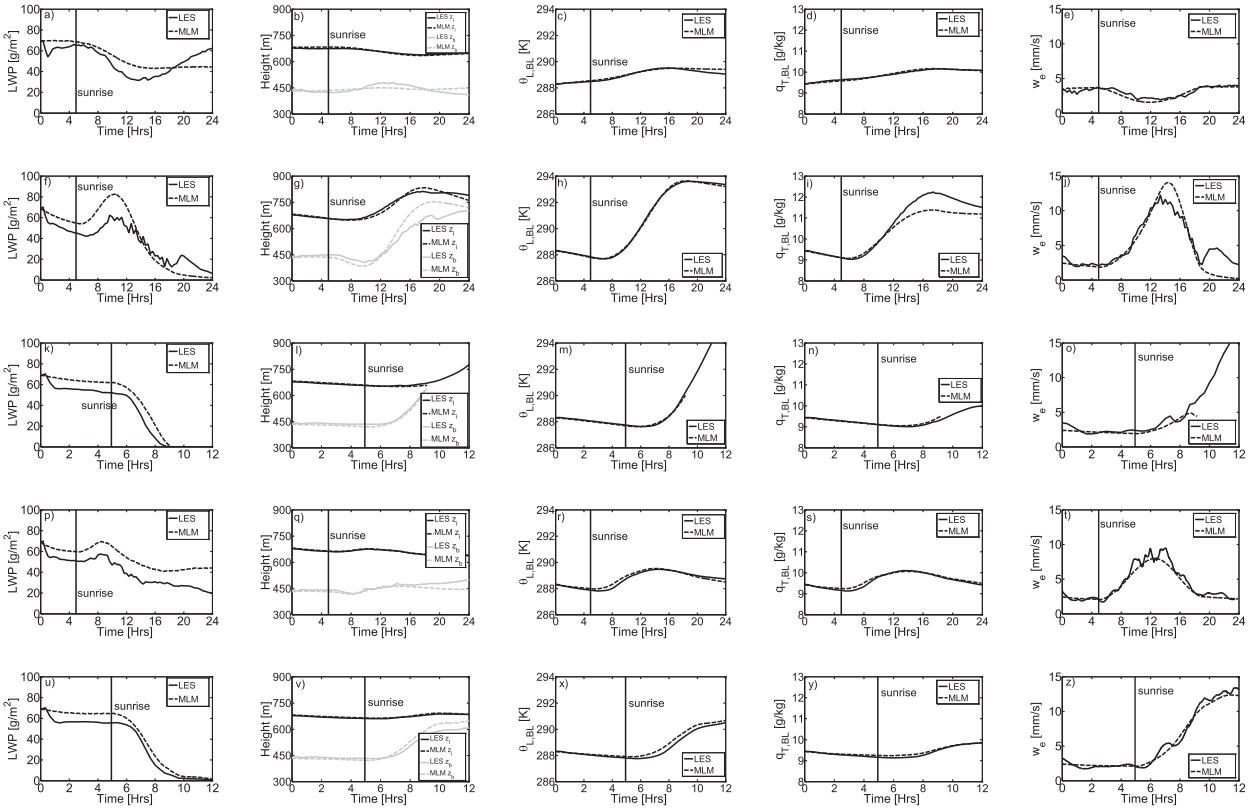

FIG. 7. Comparison between LES (solid) and MLM (dashed) for the CGILS case of (a),(f),(k),(p),(u) LWP, (b),(g),(l),(q),(v) cloud base (gray) and inversion height (black), (c),(h),(m),(r),(x) liquid potential temperature of the boundary (θ_{BL}), (d),(i),(n),(s),(y) total water mixing ratio ($q_{T\mathrm{BL}}$), and (e),(j),(o),(t),(z) entrainment velocity (w_e) for (a)–(e) the ocean case, (f)–(j) land case with Bowen ratio equal 0.1, (k)–(o) land case with Bowen ratio equal 1.0, (p)–(t) coupled case with horizontal advection representing the diurnally varying sea breeze circulation and Bowen ratio equal to 0.1, and (u)–(z) coupled case with horizontal advection representing the diurnally varying sea breeze circulation and Bowen ratio equal to 1.0. Note that for (k)–(o) the land case with Bowen ratio equal to 1.0 and (u)–(z) coupled case with Bowen ratio equal to 1.0, the plots are only from 0000 to 1200 LST as the cloud dissipates soon after sunrise and the MLM simulation ends.

thermodynamic profiles sampled after the spinup period (not shown). However, we choose to use the CGILS profiles rather than the postspinup LES profiles to initialize the MLM as our goal is to develop a stand-alone MLM. Note that surface fluxes agree exactly because the same ocean surface model is used in the LES and MLM. The moistening effect of surface latent heat flux is stronger than the heating effect of sensible heat flux over the ocean, resulting in net cloud thickening. Subsidence thins the cloud by pushing the inversion downward (Myers and Norris 2013). Entrainment flux, on the other hand, modulates cloud thickness and lifetime by raising the cloud top and thinning the cloud layer through the mixing of warm dry air aloft into the clouds. The magnitude of entrainment flux decreases during the day over the ocean owing to the decrease in buoyancy flux caused by solar heating that offsets the longwave cooling within the cloud layer.

b. *Land cases without advection—Effects of surface conditions on cloud lifetime*

At night over land, longwave cooling is the main factor driving turbulence and entrainment flux. During day, surface flux is an additional source of turbulence and heating and moistening. For the wet surface case (small Bowen ratio), the stratocumulus layer breaks up at 1400 LST followed by partly cloudy conditions until sunset, after which the cloud cover returns to overcast (Figs. 5d–f). The increase in surface latent heat flux after sunrise moistens the STBL (Fig. 5e). The surface buoyancy flux (refer to section 4b, Fig. 6d) keeps the STBL well mixed despite the increase in inversion height by more than 100 m between sunrise and midday (Fig. 6c). LWP is greater in the MLM than the LES, possibly because of the LWP loss during LES spinup. Consequently, the higher LWP in the MLM attenuates the net surface radiation, thereby reducing the surface turbulent flux

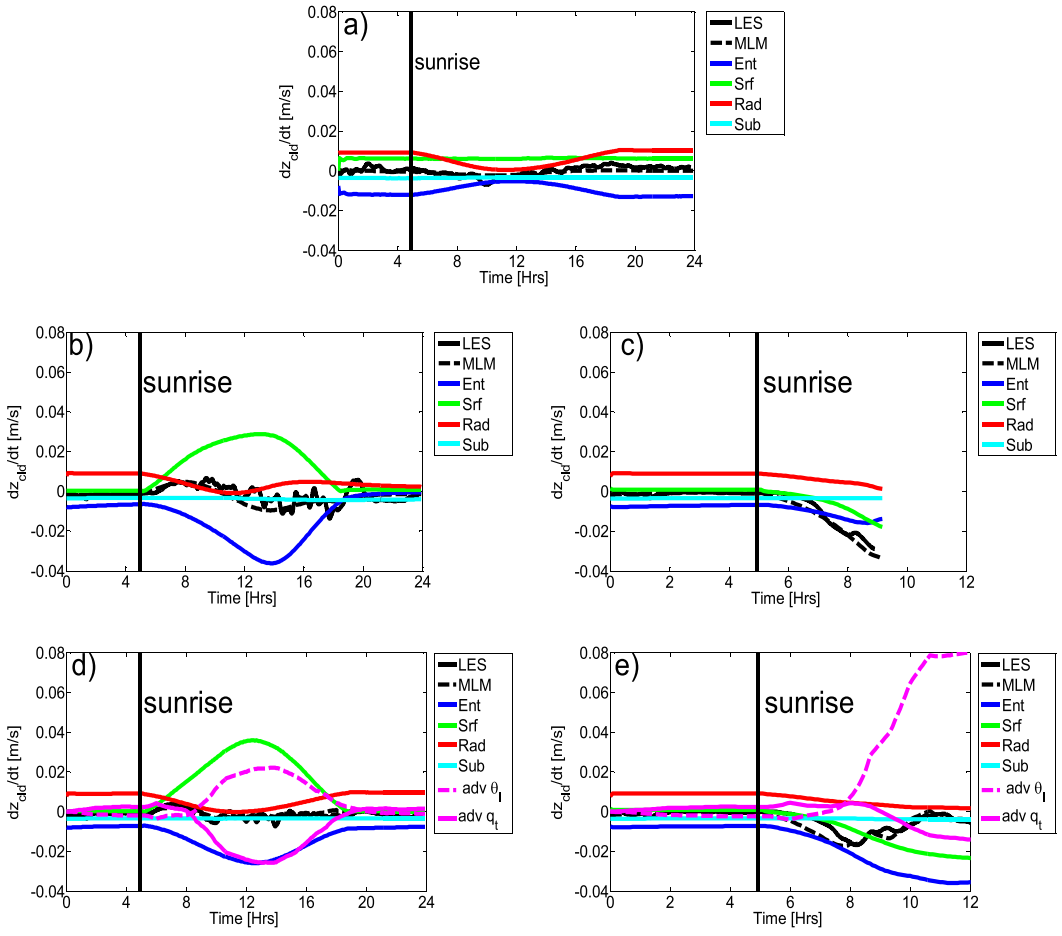

FIG. 8. Breakdown of the different factors controlling cloud thickness (h) evolution in the MLM for (a) the ocean case, the land surface case with Bowen ratio equal to (b) 0.1 and (c) 1.0, and the coupled case with Bowen ratio equal to (d) 0.1 and (e) 1.0. The entrainment flux across the inversion is denoted by the blue line, SHF ($\rho c_p \overline{w'\theta'_{l0}}$) and LHF ($\rho L \overline{w'q'_{T0}}$) by the green line, radiation divergence by the red line, subsidence by the cyan line, large-scale horizontal advection of heat by the dashed magenta line, the large-scale horizontal advection of moisture by the solid magenta line, and total cloud thickness tendency by the solid black line for LES and the dashed black line for MLM.

(Figs. 7f,k). In particular, the lower latent heat flux in the MLM results in lower STBL moisture content later in the day compared to the LES (Fig. 7i). Despite the substantial moistening effect of surface latent heat flux, the combination of solar absorption and enhanced entrainment flux thin the cloud at a faster rate than the surface latent heat flux thickens the cloud; thus, the cloud layer eventually dissipates in the MLM (Fig. 8b).

For the dry surface case (large Bowen ratio), we observe rapid cloud dissipation soon after sunrise as the STBL substantially warms because of increasing surface sensible heat flux (Figs. 5g–i). The sensible heat flux drives a strong increase in buoyancy flux (Fig. 6e), resulting in a rapidly increasing entrainment velocity that incorporates more warm dry air aloft into the STBL (Fig. 7o). Stronger warm thermals emitted by the dry land surface substantially enhance STBL height compared to the wet surface case. Pal and Haeffelin (2015) similarly found that inversion height evolution, measured using lidar, had a higher correlation to land surface processes for drier soil conditions. The MLM overestimates LWP compared to the LES, but the difference in cloud lifetime is less than 30 min (Figs. 7k–o). In both simulations, the combination of increasing sensible heat flux and entrainment flux dissipate the cloud shortly after sunrise (Fig. 8c).

c. *Land case with advection of oceanic air—Effects of large-scale horizontal advection on cloud lifetime*

Similar to the prior cases, the MLM has larger LWP than the LES as a result of spinup effects causing a drop in LWP within the first 2 h for the LES. Thermodynamic values (θ_l, q_T) and entrainment are in good agreement between both simulations (Figs. 7p–z). In both the wet

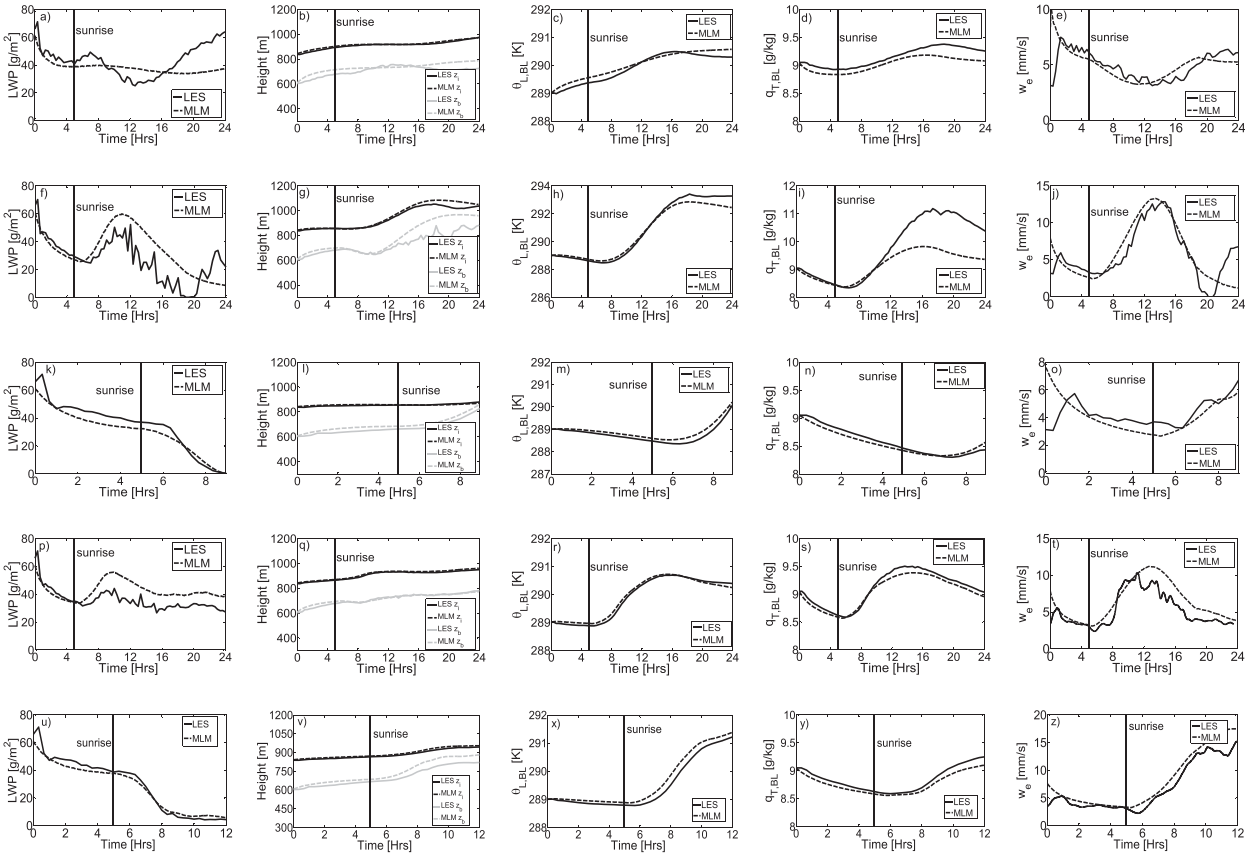

FIG. 9. As in Fig. 7, but for the DYCOMS initial conditions.

and dry surface coupled cases the cloud layer is mainly controlled by radiation and entrainment flux during the night, similar to the land case without large-scale horizontal advection. Advective cooling and drying are about balanced at night. During the day the prescribed horizontal winds increase as a result of the pressure difference between the warm land and cool ocean air masses (Fig. 4). Combined with the temperature and moisture differences between both air masses, the winds give rise to the advective tendencies.

In terms of temperature, large-scale advection of ocean air produces a strong cooling effect after sunrise that thickens the cloud layer for both dry and wet land surface conditions. In terms of moisture, large-scale advection acts to thin the cloud layer for the wet surface case (Fig. 8d). This is because the land STBL experiences increased latent heat flux from a wet surface at warmer temperature and thus has greater water vapor mixing ratio than air advected from the ocean. The combined effects of large-scale advection of heat and moisture nonetheless provide a net cloud thickening, as expected. Consequently, the cloud layer in the coupled wet land surface case exists in a cooler STBL and persists throughout the day (Figs. 5j–l), unlike the wet land surface case without advection. The cloud thickening effect of horizontal advection of cooler air (with lower saturation mixing ratio) offsets the cloud thinning effects of larger entrainment flux, solar absorption, and the lower mixing ratio of the advected air (Fig. 8d).

For the coupled dry surface case, the clouds dissipate during the day and reform after sunset (Fig. 5o). This case is similar to stratocumulus clouds occurring over the relatively dry Southern California coast during the summer months (Fig. 1). The STBL does not warm as fast in the coupled case as in the uncoupled land case because cooling from large-scale advection acts to offset the strong warming effect of entrainment flux, surface sensible heat flux, and solar absorption. The reduced warming of the STBL results in slower cloud dissipation. The cloud layer begins to thin at 0900 LST, resulting in a broken cloud deck (cumulus clouds) that persists until 1230 LST, followed by clear skies (Figs. 7u–z). The cloud thickening effect of large-scale advection is further enhanced by the attenuation of net surface radiation by the thicker cloud, thus reducing energy available for the surface flux warming. The advective tendencies more

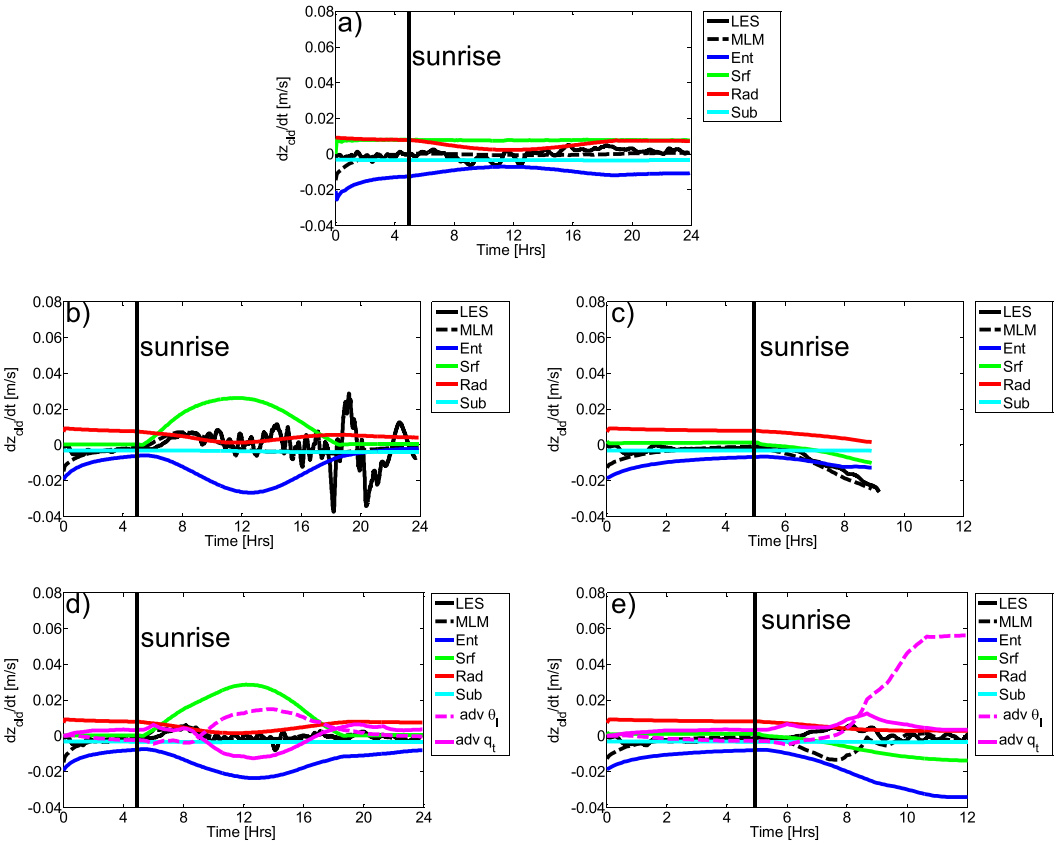

FIG. 10. As in Fig. 8, but for the DYCOMS initial conditions.

strongly support cloud thickening in the dry case compared to the wet case, because (i) the STBL over dry land is warmer, thus increasing land–ocean temperature gradients, and (ii) the STBL over dry land is less moist and therefore advection only causes minimal drying compared to the STBL over wet land.

Fluctuations in coastal wind speed and direction at subhour temporal and 1–10-km spatial scales resulting from variations in ocean–land pressure differences and synoptic conditions could be responsible for the observed day-to-day and spatial differences in stratocumulus cloud cover along the coast. This was observed during the Variability of the American Monsoon Systems Ocean–Cloud–Atmosphere–Land Study Regional Experiment (VOCALS-REx) campaign in which horizontal advection had a strong effect on marine boundary layer height and the advection term ($\overline{\boldsymbol{v}}$) could reach 15 mm s^{-1} (Rahn and Garreaud 2010).

d. *DYCOMS cases—Effects of initial conditions on cloud lifetime*

To test how well the MLM performs under different initial conditions and the different physical factors affecting cloud lifetime, we simulate the five cases using DYCOMS initial profiles that consist of higher inversion height and a stronger temperature inversion than that of CGILS (Fig. 3). The LES and MLM results for the DYCOMS case are in good agreement (Fig. 9). In the first 2 h of the DYCOMS case, the MLM overpredicts entrainment velocity compared to the LES owing to a relatively weaker inversion and a stronger entrainment efficiency coefficient, and the stronger entrainment flux causes a rapid decrease in LWP in the MLM that is comparable to the decrease in LES due to the spinup effect. The major difference between the CGILS and DYCOMS cases is that the entrainment velocities are higher in the DYCOMS cases (Figs. 9e,j,o,t,z) than in the CGILS cases (Figs. 7e,j,o,t,z) because of the weaker inversion in DYCOMS initial profile (Fig. 3). Hence, the inversion height increases at a faster rate in the DYCOMS cases compared to the CGILS cases. Despite the higher magnitude of entrainment velocity in the DYCOMS cases, the contribution of entrainment flux to cloud thinning is similar to CGILS (Figs. 8 and 10) owing to the weaker temperature inversion in the DYCOMS case. Despite the difference in initial conditions, the cloud lifetime in both cases behaves similarly in response to the external forcings such as land surface properties and large-scale horizontal advection.

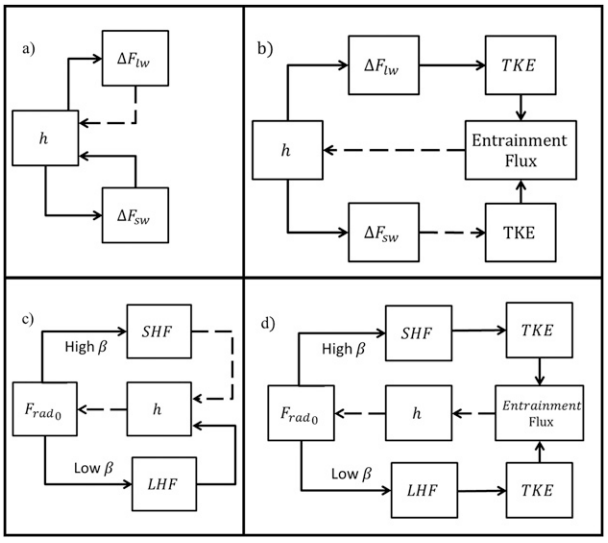

FIG. 11. Feedback loops acting upon the cloud thickness h in the MLM. Solid lines denote positive effects, and dashed lines denote negative effects. Feedback loops are shown separately for (a) radiative divergence, (b) entrainment driven by radiative divergence, (c) surface flux, and (d) surface flux driven by radiative divergence.

e. *STBL feedback loops*

The advantage of Eq. (16) applied to a MLM is that we can map the feedbacks between two variables and the interaction between different feedbacks. Although we provide only a qualitative description of the main feedback loops present in the STBL over the coast in this section, the feedback analysis could be expanded to include a quantitative analysis similar to that of Jones et al. (2014), in which the authors used LES and MLM to quantify the adjustment time scale arising from cloud thickness–turbulence–entrainment feedbacks for stratocumulus clouds over the ocean. A positive effect is one in which change (increase or decrease) in a certain variable results in the same type of change (increase or decrease) in a second variable and vice versa for a negative effect. Effects can then be summed to form feedback loops. A positive feedback (reinforcing) loop occurs when a change in a certain variable ultimately comes back to cause further change in the same direction for that certain variable. A negative (balancing) loop, on the other hand, occurs when a change in a certain variable ultimately comes back to cause change in the opposite direction for that certain variable. An example of a positive loop is when the surface sensible heat flux warms the boundary layer and dissipates the cloud layer, thereby increasing the net surface radiation, which feeds the surface flux. An example of a negative feedback loop is when the surface latent heat flux moistens the boundary layer, thereby thickening the cloud layer and reducing the net surface radiation feeding the surface latent heat flux. For the STBL particularly over land, the daytime cloud dissipating feedback loops tend to be more powerful, leading to rapid thinning of the initial cloud layer.

For all five cases, longwave radiative divergence cools the STBL, thereby thickening the cloud layer and increasing the longwave radiative divergence across the cloud layer, thus forming a reinforcing feedback loop (Fig. 11a). Longwave radiative divergence additionally drives the turbulence in the STBL, which feeds cloud-top entrainment which in turn warms and dries the STBL, thereby reducing the cloud thickness and the longwave radiative divergence and thus forming a negative feedback loop (Fig. 11b). Nocturnally, we observe that the stabilizing longwave radiation–entrainment feedback loop dominates and that the LW cooling of the BL saturates for LWPs of around 40 g m^{-2} (Figs. 7a and 9a).

Over the ocean, solar radiative heating has two opposing effects on cloud thickness: (i) warming of the STBL that thins the cloud and therefore reduces solar heating within the cloud layer (balancing feedback loop) and (ii) warming of the cloud layer that opposes longwave cooling and reduces buoyancy flux, which reduces cloud thinning due to weaker entrainment flux (positive feedback loop; Figs. 11a,b). Over land, the STBL responds much faster to solar heating because the lower heat capacity of the land surface means most of the net surface radiative flux is reemitted by the land surface as turbulent fluxes of sensible and latent heat. Large-scale horizontal advection acts to dampen the effects of solar heating by thickening the cloud layer, thereby reducing the net radiation at the surface.

For the low Bowen ratio case we have two feedback loops: (i) a negative feedback loop that maintains the cloud layer and consists of surface latent heat flux moistening the STBL, thickening the cloud, and thereby attenuating the surface radiation feeding the surface flux and (ii) a positive feedback loop that causes the cloud to dissipate and consists of latent heat flux feeding the cloud-top entrainment flux, dissipating the cloud layer, and thereby increasing surface radiation feeding the surface flux (Figs. 11c,d). We observe a positive feedback loop, in the high Bowen ratio case, in which increased sensible heat flux leads to increased entrainment with both factors then warming and drying the STBL. Both factors decrease the LWP, which in turn increases the net solar radiative flux at the surface thus driving an additional increase of surface flux (Fig. 11d).

6. Conclusions

We employed LES and a MLM to investigate factors controlling stratocumulus clouds over coastal land in general and the timing of daytime cloud dissipation in particular. One necessary development that we expect will improve MLM simulations over land is the parameterization of the entrainment velocity as function of the surface buoyancy flux and the integrated cloud buoyancy flux. The simulated STBL and cloud dissipation time in the MLM was found to be in good agreement with LES results. In particular, the entrainment scheme produced entrainment velocities and inversion heights consistent with the LES results for a variety of cases, including over ocean.

We found that cloud lifetime is sensitive to land surface conditions characterized by the Bowen ratio since the bulk of the net surface radiation over land is converted to convective fluxes into the boundary layer. For wet land surfaces, latent heat flux dominates over sensible heat flux, thus moistening the STBL and thereby thickening the cloud layer. In contrast, for moderately dry surfaces, the sensible heat flux dominates, and it and entrainment flux act together to rapidly dissipate the cloud after sunrise. The stronger surface buoyancy fluxes for both wet and dry land cases (compared to the ocean) indirectly thin the cloud by increasing turbulence in the STBL and increasing the cloud-top entrainment flux. Furthermore, the surface net radiation induces stronger surface buoyancy fluxes and stronger entrainment at larger Bowen ratios.

The sea breeze is an important feature of coastal environments, and onshore winds advect cool air from over the ocean onto the coast, thereby thickening the cloud layer. We represented advection effects by prescribing wind speed obtained from surface wind measurements and using temperature and humidity outputs from LES and MLM simulations over the ocean. The advection of ocean air onto the coast plays an important role in modulating the cloud lifetime. For both dry and wet land surface conditions, large-scale horizontal advection cools and dries the STBL. For the wet surface case, the large-scale horizontal advective cooling contributes to maintenance of the cloud layer throughout the day. For the dry surface case with advection, cloud dissipation time is delayed by roughly 3 h.

We believe that this study and future applications of the MLM modified turbulence and entrainment parameterizations will provide important insights into the factors controlling stratocumulus cloud lifetime over coastal land. This study has additionally highlighted the differences between STBL occurring over oceans and coastal lands. Hence, parameterizations developed for stratocumulus clouds over the ocean might not succeed in capturing the physics of those clouds occurring over coastal lands. An analysis benchmarking the capability of the different parameterizations, notably entrainment, in representing the STBL over coastal lands remains to be explored in future work.

Acknowledgments. We acknowledge funding from the California Solar Initiative RD&D program. The authors thank Patrick Mathiesen for providing the Normalized GHI observations at the University of California, San Diego in Fig. 1 and Handa Yang for processing the SolarAnywhere data.

APPENDIX A

Mixed-Layer Model Governing Equations

The boundary layer columnar mass ($m_{\text{clm}} = \overline{\rho}_{\text{air}} z_i$, where $\overline{\rho}_{\text{air}}$ represents the density of air and z_i is the inversion height) balance equation is formulated as

$$\frac{\partial z_i}{\partial t} + \upsilon_H \cdot \nabla z_i = w_e + w_s(z_i) = w_e - D z_i . \quad \text{(A1)}$$

We have assumed that the density remains constant up to the inversion height as STBL inversion heights are usually much less than 2 km. The first and second terms on the left-hand side of Eq. (A1) represent the STBL columnar mass tendency and large-scale horizontal advection, respectively. The first term on the right-hand side of Eq. (A1) represents the entrainment rate and the second the vertical large-scale wind component (subsidence), which is taken to be a function of inversion height and divergence D. Note that $\overline{\rho}_{\text{air}}$ cancels out on both sides of the equation.

The heat budget equation is formulated in terms of the liquid potential temperature ($\theta_l = \theta - (1/\Pi)(L_v/c_p) q_l$), where q_l represents the liquid water mixing ratio, θ represents the potential temperature, $\Pi = (P/P_0)^{R_d/c_p}$ is the Exner function, L_v is the latent heat of evaporation, c_p is the specific heat of air at constant pressure, and R_d is the dry-air gas constant.

The MLM heat and moisture budget equations were derived in detail by Lilly (1968) and more recently by Caldwell et al. (2005). The final budget equations are expressed as

$$\frac{\partial \overline{\theta}_{l\text{BL}}}{\partial t} + (\overline{\boldsymbol{v}} \cdot \nabla_h \overline{\theta}_l)_{\text{BL}} = -\frac{\partial}{\partial z}\left[\overline{w'\theta'_l}(z) + \frac{F_{\text{rad}}(z)}{c_p \rho_{\text{air}}}\right] = \frac{1}{z_i}\left(\overline{w'\theta'_{l0}} + w_e \Delta\theta_{li} - \frac{\Delta F_{\text{rad}}}{c_p \rho_{\text{air}}}\right) \quad \text{(A2)}$$

and

$$\frac{\partial \overline{q_T}_{\mathrm{BL}}}{\partial t} + (\overline{\boldsymbol{v}} \cdot \nabla_h \overline{q_T})_{\mathrm{BL}} = -\frac{\partial \overline{w'q'_T}(z)}{\partial z} = \frac{1}{z_i}(\overline{w'q'_{T0}} + w_e \Delta q_{Ti}), \tag{A3}$$

where ∇_h is the horizontal divergence operator and $(\overline{\boldsymbol{v}} \cdot \nabla_h \overline{\theta_l})_{\mathrm{BL}}$, $(\overline{\boldsymbol{v}} \cdot \nabla_h \overline{q_T})_{\mathrm{BL}}$ represent the large-scale horizontal advection of heat and moisture into the boundary layer, respectively. The terms $\overline{w'\theta'_l}_0$ and $\overline{w'q'_T}_0$ are the surface sensible and latent heat flux, respectively. The variable ΔF_{rad} represents the net radiation divergence across the cloud. Precipitation is neglected in the MLM formulation as the clouds are assumed to be thin enough not to precipitate or drizzle significantly. The terms $\Delta\theta_l = \theta_{li} - \overline{\theta_l}_{\mathrm{BL}}$ and $\Delta q_T = q_{Ti} - \overline{q_T}_{\mathrm{BL}}$ represent the inversion jumps for heat and moisture, respectively (see also section 4c). Here $\overline{\theta_l}_{\mathrm{BL}}$ and $\overline{q_T}_{\mathrm{BL}}$ represent the STBL-averaged liquid potential temperature and total water mixing ratio, respectively, while θ_{li} and q_{ti} are evaluated just above the inversion height.

As in CGILS S12, we specify the free tropospheric liquid potential temperature profiles as

$$\theta_{li} = \theta_{li}(0) + (5.22\,\mathrm{K\,km^{-1}})z_i, \tag{A4}$$

with $\theta_{li}(0) = 299\,\mathrm{K}$, while for DYCOMS

$$\theta_{li} = \theta_{li}(0) + (8.56\,\mathrm{K\,km^{-1}})z \tag{A5}$$

and $\theta_{li}(0) = 293.5\,\mathrm{K}$. The variable q_{Ti} is constant in height above the inversion and is set as $3.5\,\mathrm{g\,kg^{-1}}$ for the CGILS case and $1.5\,\mathrm{g\,kg^{-1}}$ for the DYCOMS case.

To compute surface flux we employ an LSM identical to that utilized in the LES (outlined in section 3b). To obtain the large-scale advection terms, similar to the LES, we specify

$$\overline{\boldsymbol{v}} \cdot \nabla_h \overline{z_i} = \overline{\boldsymbol{v}} \cdot [\overline{z_i}_{\mathrm{land}}(t) - \overline{z_i}_{\mathrm{ocean}}(t)]/\Delta x, \tag{A6a}$$

$$\overline{\boldsymbol{v}} \cdot \nabla_h \overline{\theta_l} = \overline{\boldsymbol{v}} \cdot [\overline{\theta_l}_{\mathrm{land_{BL}}}(t) - \overline{\theta_l}_{\mathrm{ocean_{BL}}}(t)]/\Delta x, \quad \text{and} \tag{A6b}$$

$$\overline{\boldsymbol{v}} \cdot \nabla_h \overline{q_T} = \overline{\boldsymbol{v}} \cdot [\overline{q_T}_{\mathrm{land_{BL}}}(t) - \overline{q_T}_{\mathrm{ocean_{BL}}}(t)]/\Delta x, \tag{A6c}$$

where $\overline{\theta_l}_{\mathrm{ocean_{BL}}}(t)$, $\overline{q_T}_{\mathrm{ocean_{BL}}}(t)$ and $\overline{z_i}_{\mathrm{ocean}}(t)$ represent the ocean boundary layer liquid potential temperature, total water mixing ratio, and inversion height, respectively, obtained from the ocean MLM case. Within the MLM $\overline{\theta_l}_{\mathrm{land_{BL}}}(t)$, $\overline{q_T}_{\mathrm{land_{BL}}}(t)$, and $\overline{z_i}_{\mathrm{land}}(t)$ are computed dynamically. Note that the MLM is a zero-dimensional model and hence the temperature and moisture are values are assumed to be height independent within the STBL.

APPENDIX B

Parameterization of Longwave Radiation for the MLM

To develop a longwave radiative flux model that accounts for the large temperature differences between land surface and cloud typically observed in an STBL over land, we first assume an idealized cloud with the following properties: horizontally infinite uniform slab, constant asymmetry factor g, single scattering albedo ω, mass extinction cross section m, and temperature T. Following Goody (1995) and Larson et al. (2007), the net radiative flux is expressed as

$$\frac{d^2F}{d\tau^2} = \alpha^2 F, \quad \alpha^2 = 3(1-\omega)(1-\omega g), \tag{B1}$$

with the following boundary conditions at the cloud top

$$\frac{dF}{d\tau}_{\tau=0} = 4\pi(1-\omega)\left[\frac{F_{\tau=0}}{2\pi} - (B_{\mathrm{cld}} - B_t)\right] \tag{B2}$$

and the cloud bottom

$$\frac{dF}{d\tau}_{\tau=\tau_b} = 4\pi(1-\omega)\left[(B_b - B_{cld}) - \frac{F_{\tau=\tau_b}}{2\pi}\right]. \tag{B3}$$

In Eq. (B3) B_b is the upwelling blackbody radiance at the cloud base $[B_b = (\sigma/\pi)T_{\mathrm{srf}}^4]$, where T_{srf} is the surface temperature that is determined dynamically from the land surface model. In addition, B_{cld} is the blackbody emitted radiance from the cloud $[B_{\mathrm{cld}} = (\sigma/\pi)T_{\mathrm{cld}}^4]$ where T_{cld} is the effective cloud temperature that is obtained dynamically from the MLM, and B_t is the downwelling blackbody radiance at the cloud top $[B_t = (\sigma/\pi)T_t^4]$, where T_t is the effective temperature of the air just above the cloud and σ is the Stefan–Boltzmann constant. The solution to Eq. (B1) determined by inspection is

$$F = Le^{\alpha\tau} + Me^{-\alpha\tau}. \tag{B4}$$

By substituting Eq. (B4) into the boundary conditions [Eqs. (B2) and (B3)], L and M are determined as

$$L = \gamma[(B_{\mathrm{cld}} - B_t)c_1 e^{-\alpha\tau_b} + (B_0 - B_{\mathrm{cld}})c_2] \quad \text{and}$$
$$M = \gamma[(B_{\mathrm{cld}} - B_t)c_2 e^{\alpha\tau_b} + (B_0 - B_{\mathrm{cld}})c_1], \tag{B5}$$

where

$$\gamma = -\frac{4\pi(1-\omega)}{c_1^2 e^{-\alpha\tau_b} - c_2^2 e^{\alpha\tau_b}}, \tag{B6}$$

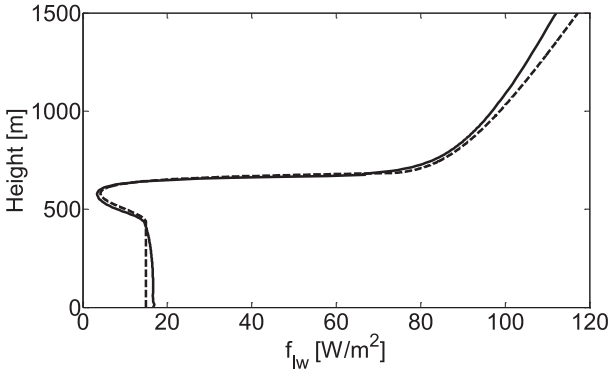

FIG. B1. Comparison of longwave radiation derived from LES (solid) and MLM (dashed) computed using the CGILS S12 temperature and liquid water vertical profiles.

and

$$c_1 = \alpha - 2(1-\omega) \quad \text{and}$$
$$c_2 = \alpha + 2(1-\omega). \tag{B7}$$

Finally, following Stevens et al. (2005), Eq. (B4) is augmented to include cooling of the air above the cloud top as

$$F_{\mathrm{LW}} = Le^{\alpha\tau} + Me^{-\alpha\tau} + \rho_{\mathrm{air},i} c_p D \alpha_z \left[\frac{(z-z_i)^{4/3}}{4} + z_i (z-z_i)^{1/3} \right], \tag{B8}$$

where $\rho_{\mathrm{air},i}$ is the density of air at the inversion and $\alpha_z = 1\,\mathrm{m}^{-4/3}$. The value of D equals 4.86×10^{-6} or $3.75 \times 10^{-6}\,\mathrm{s}^{-1}$, which represents large-scale divergence for the CGILS and DYCOMS cases, respectively. Thus, the first term in Eq. (B8) represents the cloud-top cooling, the second the cloud-base warming, and the third the cooling in the troposphere and is only applied above the inversion. The parameterized longwave radiation was found to be in agreement with that computed in LES using the Monte Carlo spectral radiation scheme (Pincus and Stevens 2009; Fig B1).

REFERENCES

Ackerman, A. S., and Coauthors, 2009: Large-eddy simulations of a drizzling, stratocumulus-topped marine boundary layer. *Mon. Wea. Rev.*, **137**, 1083–1110, doi:10.1175/2008MWR2582.1.

Albrecht, B. A., C. Fairall, D. W. Thomson, and A. B. White, 1990: Surface-based remote sensing of the observed and the adiabatic liquid water content of stratocumulus clouds. *Geophys. Res. Lett.*, **17**, 89–92, doi:10.1029/GL017i001p00089.

Blossey, P. N., and Coauthors, 2013: Marine low cloud sensitivity to an idealized climate change: The CGILS LES intercomparison. *J. Adv. Model. Earth Syst.*, **5**, 234–258, doi:10.1002/jame.20025.

Bony, S., and J.-L. Dufresne, 2005: Marine boundary layer clouds at the heart of tropical cloud feedback uncertainties in climate models. *Geophys. Res. Lett.*, **32**, L20806, doi:10.1029/2005GL023851.

Bretherton, C., and M. C. Wyant, 1997: Moisture transport, lower-tropospheric stability, and decoupling of cloud-topped boundary layers. *J. Atmos. Sci.*, **54**, 148–167, doi:10.1175/1520-0469(1997)054<0148:MTLTSA>2.0.CO;2.

——, S. Krueger, M. Wyant, P. Bechtold, E. Van Meijgaard, B. Stevens, and J. Teixeira, 1999: A GCSS boundary-layer cloud model intercomparison study of the first Astex Lagrangian experiment. *Bound.-Layer Meteor.*, **93**, 341–380, doi:10.1023/A:1002005429969.

——, P. N. Blossey, and C. R. Jones, 2013: Mechanisms of marine low cloud sensitivity to idealized climate perturbations: A single-LES exploration extending the CGILS cases. *J. Adv. Model. Earth Syst.*, 316–337, doi:10.1002/jame.20019.

Caldwell, P., C. S. Bretherton, and R. Wood, 2005: Mixed-layer budget analysis of the diurnal cycle of entrainment in Southeast Pacific stratocumulus. *J. Atmos. Sci.*, **62**, 3775–3791, doi:10.1175/JAS3561.1.

Dal Gesso, S. D., A. P. Siebesma, S. R. de Roode, and J. M. van Wessem, 2014: A mixed-layer model perspective on stratocumulus steady states in a perturbed climate. *Quart. J. Roy. Meteor. Soc.*, **140**, 2119–2131, doi:10.1002/qj.2282.

Duda, D. P., G. L. Stephens, and S. K. Cox, 1991: Microphysical and radiative properties of marine stratocumulus from tethered balloon measurements. *J. Appl. Meteor.*, **30**, 170–186, doi:10.1175/1520-0450(1991)030<0170:MARPOM>2.0.CO;2.

Duynkerke, P. G., and Coauthors, 2004: Observations and numerical simulations of the diurnal cycle of the EUROCS stratocumulus case. *Quart. J. Roy. Meteor. Soc.*, **130**, 3269–3296, doi:10.1256/qj.03.139.

EPA, 2004: User's guide for the AERMOD Meteorological Preprocessor (AERMET). U.S. Environmental Protection Agency Rep. EPA-454/B-03-002, 252 pp. [Available online at https://www3.epa.gov/scram001/7thconf/aermod/aermetugb.pdf.]

Fang, M., B. Albrecht, V. Ghate, and P. Kollias, 2014a: Turbulence in continental stratocumulus, Part I: External forcings and turbulence structures. *Bound.-Layer Meteor.*, **150**, 341–360, doi:10.1007/s10546-013-9873-3.

——, ——, ——, and ——, 2014b: Turbulence in continental stratocumulus, Part II: Eddy dissipation rates and large-eddy coherent structures. *Bound.-Layer Meteor.*, **150**, 361–380, doi:10.1007/s10546-013-9872-4.

Fedorovich, E., R. Conzemius, and D. Mironov, 2004: Convective entrainment into a shear-free, linearly stratified atmosphere: Bulk models reevaluated through large eddy simulations. *J. Atmos. Sci.*, **61**, 281–295, doi:10.1175/1520-0469(2004)061<0281:CEIASL>2.0.CO;2.

Garcia, J. R., and J. P. Mellado, 2014: The two-layer structure of the entrainment zone in the convective boundary layer. *J. Atmos. Sci.*, **71**, 1935–1955, doi:10.1175/JAS-D-13-0148.1.

Ghate, V. P., B. A. Albrecht, and P. Kollias, 2010: Vertical velocity structure of nonprecipitating continental boundary layer stratocumulus clouds. *J. Geophys. Res.*, **115**, D13204, doi:10.1029/2009JD013091.

Ghonima, M. S., J. R. Norris, T. Heus, and J. Kleissl, 2015: Reconciling and validating the cloud thickness and liquid water path tendencies proposed by R. Wood and J. J. van der Dussen et al. *J. Atmos. Sci.*, **72**, 2033–2040, doi:10.1175/JAS-D-14-0287.1.

Goody, R. M., 1995: *Principles of Atmospheric Physics and Chemistry*. Oxford University Press, 336 pp.

Grenier, H., and C. S. Bretherton, 2001: A moist PBL parameterization for large-scale models and its application to

subtropical cloud-topped marine boundary layers. *Mon. Wea. Rev.*, **129**, 357–377, doi:10.1175/1520-0493(2001)129<0357:AMPPFL>2.0.CO;2.

Heus, T., and Coauthors, 2010: Formulation of the Dutch Atmospheric Large-Eddy Simulation (DALES) and overview of its applications. *Geosci. Model Dev.*, **3**, 415–444, doi:10.5194/gmd-3-415-2010.

Hilliker, J. L., and J. M. Fritsch, 1999: An observations-based statistical system for warm-season hourly probabilistic forecasts of low ceiling at the San Francisco International Airport. *J. Appl. Meteor.*, **38**, 1692–1705, doi:10.1175/1520-0450(1999)038<1692:AOBSSF>2.0.CO;2.

Iacobellis, S. F., and D. R. Cayan, 2013: The variability of California summertime marine stratus: Impacts on surface air temperatures. *J. Geophys. Res. Atmos.*, **118**, 9105–9122, doi:10.1002/jgrd.50652.

Ineichen, P., and R. Perez, 2002: A new airmass independent formulation for the Linke turbidity coefficient. *Sol. Energy*, **73**, 151–157, doi:10.1016/S0038-092X(02)00045-2.

Jones, C. R., C. S. Bretherton, and P. N. Blossey, 2014: Fast stratocumulus timescale in mixed layer model and large eddy simulation. *J. Adv. Model. Earth Syst.*, **6**, 206–222, doi:10.1002/2013MS000289.

Joseph, J. H., W. J. Wiscombe, and J. A. Weinman, 1976: The Delta-Eddington approximation for radiative flux transfer. *J. Atmos. Sci.*, **33**, 2452–2459, doi:10.1175/1520-0469(1976)033<2452:TDEAFR>2.0.CO;2.

Kazil, J., G. Feingold, and T. Yamaguchi, 2015: Wind speed response of marine non-precipitating stratocumulus clouds over a diurnal cycle in cloud-system resolving simulations. *Atmos. Chem. Phys. Discuss.*, **15**, 28 395–28 452, doi:10.5194/acpd-15-28395-2015.

Klein, S. A., and D. L. Hartmann, 1993: The seasonal cycle of low stratiform clouds. *J. Climate*, **6**, 1587–1606, doi:10.1175/1520-0442(1993)006<1587:TSCOLS>2.0.CO;2.

Kollias, P., and B. Albrecht, 2000: The turbulence structure in a continental stratocumulus cloud from millimeter-wavelength radar observations. *J. Atmos. Sci.*, **57**, 2417–2434, doi:10.1175/1520-0469(2000)057<2417:TTSIAC>2.0.CO;2.

Larson, V. E., K. E. Kotenberg, and N. B. Wood, 2007: An analytic longwave radiation formula for liquid layer clouds. *Mon. Wea. Rev.*, **135**, 689–699, doi:10.1175/MWR3315.1.

Leon, D. C., Z. Wang, and D. Liu, 2008: Climatology of drizzle in marine boundary layer clouds based on 1 year of data from CloudSat and Cloud-Aerosol Lidar and Infrared Pathfinder Satellite Observations (CALIPSO). *J. Geophys. Res.*, **113**, D00A14, doi:10.1029/2008JD009835.

Lilly, D. K., 1968: Models of cloud-topped mixed layers under a strong inversion. *Quart. J. Roy. Meteor. Soc.*, **94**, 292–309, doi:10.1002/qj.49709440106.

Mathiesen, P., and J. Kleissl, 2011: Evaluation of numerical weather prediction for intra-day solar forecasting in the continental United States. *Sol. Energy*, **85**, 967–977, doi:10.1016/j.solener.2011.02.013.

Mechem, D. B., Y. L. Kogan, and D. M. Schultz, 2010a: Large-eddy observation of post-cold-frontal continental stratocumulus. *J. Atmos. Sci.*, **67**, 3368–3383, doi:10.1175/2010JAS3389.1.

——, ——, and ——, 2010: Large-eddy simulation of post-cold-frontal continental stratocumulus. *J. Atmos. Sci.*, **67**, 3835–3853, doi:10.1175/2010JAS3467.1.

Mellado, J. P., 2010: The evaporatively driven cloud-top mixing layer. *J. Fluid Mech.*, **660**, 5–36, doi:10.1017/S0022112010002831.

Myers, T. A., and J. R. Norris, 2013: Observational evidence that enhanced subsidence reduces subtropical marine boundary layer cloudiness. *J. Climate*, **26**, 7507–7524, doi:10.1175/JCLI-D-12-00736.1.

Nicholls, S., 1984: The dynamics of stratocumulus: Aircraft observations and comparisons with a mixed layer model. *Quart. J. Roy. Meteor. Soc.*, **110**, 783–820, doi:10.1002/qj.49711046603.

——, and J. D. Turton, 1986: An observational study of the structure of stratiform cloud sheets: Part II. Entrainment. *Quart. J. Roy. Meteor. Soc.*, **112**, 461–480, doi:10.1002/qj.49711247210.

Pal, S., and M. Haeffelin, 2015: Forcing mechanisms governing diurnal, seasonal, and interannual variability in the boundary layer depths: Five years of continuous lidar observations over a suburban site near Paris. *J. Geophys. Res. Atmos.*, **120**, 11 936–11 956, doi:10.1002/2015JD023268.

Pincus, R., and B. Stevens, 2009: Monte Carlo spectral integration: A consistent approximation for radiative transfer in large eddy simulations. *J. Adv. Model. Earth Syst.*, **1** (1), doi:10.3894/JAMES.2009.1.1.

Price, J. D., 1999: Observations of stratocumulus cloud break-up over land. *Quart. J. Roy. Meteor. Soc.*, **125**, 441–468, doi:10.1002/qj.49712555404.

Rahn, D. A., and R. Garreaud, 2010: Marine boundary layer over the subtropical southeast Pacific during VOCALS-REx—Part 2: Synoptic variability. *Atmos. Chem. Phys.*, **10**, 4507–4519, doi:10.5194/acp-10-4507-2010.

Randall, D. A., J. A. Coakley, D. H. Lenschow, C. W. Fairall, and R. A. Kropfli, 1984: Outlook for research on subtropical marine stratification clouds. *Bull. Amer. Meteor. Soc.*, **65**, 1290–1301, doi:10.1175/1520-0477(1984)065<1290:OFROSM>2.0.CO;2.

Rieck, M., C. Hohenegger, and C. C. van Heerwaarden, 2014: The influence of land surface heterogeneities on cloud size development. *Mon. Wea. Rev.*, **142**, 3830–3846, doi:10.1175/MWR-D-13-00354.1.

Sandu, I., B. Stevens, and R. Pincus, 2010: On the transitions in marine boundary layer cloudiness. *Atmos. Chem. Phys.*, **10**, 2377–2391, doi:10.5194/acp-10-2377-2010.

Savic-Jovcic, V., and B. Stevens, 2008: The structure and mesoscale organization of precipitating stratocumulus. *J. Atmos. Sci.*, **65**, 1587–1605, doi:10.1175/2007JAS2456.1.

Schwartz, R. E., A. Gershunov, S. F. Iacobellis, and D. R. Cayan, 2014: North American west coast summer low cloudiness: Broadscale variability associated with sea surface temperature. *Geophys. Res. Lett.*, **41**, 3307–3314, doi:10.1002/2014GL059825.

Shettle, E. P., and J. A. Weinman, 1970: The transfer of solar irradiance through inhomogeneous turbid atmospheres evaluated by Eddington's approximation. *J. Atmos. Sci.*, **27**, 1048–1055, doi:10.1175/1520-0469(1970)027<1048:TTOSIT>2.0.CO;2.

Skupniewicz, C. E., J. W. Glendening, and R. F. Kamada, 1991: Boundary-layer transition across a stratocumulus cloud edge in a coastal zone. *Mon. Wea. Rev.*, **119**, 2337–2357, doi:10.1175/1520-0493(1991)119<2337:BLTAAS>2.0.CO;2.

SolarAnywhere, 2014: SolarAnywhere Data. Clean Power Research 2014. [Available online at http://www.solaranywhere.com.]

Stevens, B., 2002: Entrainment in stratocumulus-topped mixed layers. *Quart. J. Roy. Meteor. Soc.*, **128**, 2663–2690, doi:10.1256/qj.01.202.

——, 2010: Cloud-top entrainment instability? *J. Fluid Mech.*, **660**, 1, doi:10.1017/S0022112010003575.

——, and Coauthors, 2003: Dynamics and Chemistry of Marine Stratocumulus—DYCOMS-II. *Bull. Amer. Meteor. Soc.*, **84**, 579–593, doi:10.1175/BAMS-84-5-579.

——, and Coauthors, 2005: Evaluation of large-eddy simulations via observations of nocturnal marine stratocumulus. *Mon. Wea. Rev.*, **133**, 1443–1462, doi:10.1175/MWR2930.1.

Sullivan, P. P., C. H. Moeng, B. Stevens, D. H. Lenschow, and S. D. Mayor, 1998: Structure of the entrainment zone capping the convective atmospheric boundary layer. *J. Atmos. Sci.*, **55**, 3042–3064, doi:10.1175/1520-0469(1998)055<3042:SOTEZC>2.0.CO;2.

Taylor, S. V., D. R. Cayan, N. E. Graham, and K. P. Georgakakos, 2008: Northerly surface winds over the eastern North Pacific Ocean in spring and summer. *J. Geophys. Res.*, **113**, D02110, doi:10.1029/2006JD008053.

Uchida, J., C. S. Bretherton, and P. N. Blossey, 2010: The sensitivity of stratocumulus-capped mixed layers to cloud droplet concentration: Do LES and mixed-layer models agree? *Atmos. Chem. Phys.*, **10**, 4097–4109, doi:10.5194/acp-10-4097-2010.

Wood, R., 2012: Stratocumulus clouds. *Mon. Wea. Rev.*, **140**, 2373–2423, doi:10.1175/MWR-D-11-00121.1.

——, C. S. Bretherton, and D. L. Hartmann, 2002: Diurnal cycle of liquid water path over the subtropical and tropical oceans. *Geophys. Res. Lett.*, **29**, 2092, doi:10.1029/2002GL015371.

Yamaguchi, T., and D. A. Randall, 2008: Large-eddy simulation of evaporatively driven entrainment in cloud-topped mixed layers. *J. Atmos. Sci.*, **65**, 1481–1504, doi:10.1175/2007JAS2438.1.

Zhang, M., C. S. Bretherton, P. N. Blossey, S. Bony, F. Brient, and J.-C. Golaz, 2012: The CGILS experimental design to investigate low cloud feedbacks in general circulation models by using single-column and large-eddy simulation models. *J. Adv. Model. Earth Syst.*, **4**, M12001, doi:10.1029/2012MS000182.

Zhu, P., B. Albrecht, and J. Gottschalck, 2001: Formation and development of nocturnal boundary layer clouds over the southern Great Plains. *J. Atmos. Sci.*, **58**, 1409–1426, doi:10.1175/1520-0469(2001)058<1409:FADONB>2.0.CO;2.